Highly Mismatched GaN$_{1-x}$Sb$_x$ Alloys: Synthesis, Structure and Electronic Properties

K. M. Yu[1,2], W. L. Sarney[3], S. V. Novikov[4], N. Segercrantz[2,5], M. Ting[2,6], M. Shaw[7], S.P. Svensson[3], R. W. Martin[7], W.Walukiewicz[2], and C. T. Foxon[4]

1. *Department of Physics and Materials Science, City University of Hong Kong, Kowloon, Hong Kong*
2. *Materials Sciences Division, Lawrence Berkeley National Laboratory, 1 Cyclotron Road, Berkeley, CA 94720 USA*
3. *US Army Research Laboratory, 2800 Powder Mill Road, Adelphi MD, 20783 USA*
4. *School of Physics and Astronomy, University of Nottingham, Nottingham NG7 2RD, UK*
5. *Department of Applied Physics, Aalto University, FI-00076 Aalto, Finland*
6. *Department of Mechanical Engineering, University of California, Berkeley, CA 94720*
7. *Department of Physics, SUPA, University of Strathclyde, Glasgow, G4 0NG, UK*

ABSTRACT

Highly mismatched alloys (HMAs) is a class of semiconductor alloys whose constituents are distinctly different in terms of size, ionicity and/or electronegativity. Electronic properties of the alloys deviate significantly from an interpolation scheme based on small deviations from the virtual crystal approximation. Most of the HMAs were only studied in a dilute composition limit. Recent advances in understanding of the semiconductor synthesis processes allowed growth of thin films of HMAs under non-equilibrium conditions. Thus reducing the growth temperature allowed synthesis of group III-N-V HMAs over almost the entire composition range. This paper focuses on the GaN$_x$Sb$_{1-x}$ HMA which has been suggested as a potential material for solar water dissociation devices. Here we review our recent work on the synthesis, structural and optical characterization of GaN$_{1-x}$Sb$_x$ HMA. Theoretical modeling studies on its electronic structure based on the band anticrossing (BAC) model are also reviewed. In particular we discuss the effects of growth temperature, Ga flux and Sb flux on the incorporation of Sb, film microstructure and optical properties of the alloys. Results obtained from two separate MBE growths are directly compared. Our work demonstrates that a large range of direct bandgap energies from 3.4 eV to below 1.0 eV can be achieved for this alloy grown at low temperature. We show that the electronic band structure of GaN$_{1-x}$Sb$_x$ HMA over the entire composition range is well described by a modified the BAC model which includes the dependence of the host matrix band edges as well as the BAC model coupling parameters on composition. We emphasize that the modified BAC model of the electronic band structure developed for the full composition of GaN$_x$Sb$_{1-x}$ is general and is applicable to any HMA.

1. Introduction

Alloying of semiconductors offers the ability to tailor the bandgap and even the conduction and valence band edge positions through the manipulation of the composition of the resulting alloy. This greatly expands the applications of these materials in electronic, optoelectronic, photovoltaic and photoelectrochemical devices. The degree to which the alloy band structure is modified with a change in composition is largely determined by the mismatch in the two endpoint materials. With advances in thin film growth techniques, an increasing array of semiconductor alloys may be synthesized with increasingly mismatched constituents. It is well known that alloys composed of two compounds of similar character can be treated within the scheme of the virtual crystal approximation (VCA), where the potential of the periodic crystal is taken as an average of the atomic potentials of the constituents [1,2,3]. Within the VCA the composition dependencies of the band gaps as well as band offsets are given by linear interpolation between the values for the end point component semiconductors. However it has been found that, in most instances, a better approximation for these dependencies is obtained assuming small deviation from the linear approximation. Thus the energy gap of a semiconductor alloy A_xB_{1-x} with band gap E_A and E_B, respectively can be well approximated by the expression:

$$E_G(x) = xE_A + (1 - x)E_B - bx(1 - x) \qquad (1)$$

where x is the composition, and b is the bowing parameter describing deviation of the band gap dependence from the linear interpolation. Typically, this approximation is acceptable only if the bowing parameter is smaller than the band gaps of the constituent materials. Note that there are ternary alloys, e.g. AlGaN [4] where the bowing parameter was found to be large and composition dependent due to local strain and built-in fields in the alloy.

Progress in preparation methods for semiconductor materials now allows synthesis of semiconductor alloys of constituents whose component atoms are distinctly different in terms of size, ionicity and/or electronegativity. The electronic properties of such highly mismatched alloys (HMAs) deviate significantly from an interpolation scheme based on small deviations from the VCA [5,6,7]. Comparing to conventional ternary or quaternary alloys which require large composition alloying to achieve band gap tuning, HMAs have the unique advantage of drastically lowering the bandgap by the substitution of a small fraction (a few percent) of anions with an isovaent element. Moreover, by selecting different anion substituents we can preferentially move the conduction band or valence band of the HMA. This is particular important for photoelectrodes for photoelectrochemical water splitting where not only the band gap but also positions of the conduction and valence band are essential for efficient operation of the device.

The most extensively studied classes of HMAs are based on group III-V and II-VI semiconductor alloys in which metallic (electronegative) anions are replaced by isovalent electronegative (metallic) atoms. A prototypical and most notable example of an HMA has been As-rich GaN_xAs_{1-x} in which a small fraction (a few percent) of highly electronegative N replaces the host As atoms. A striking feature of this alloy was a strong dependence of the band gap

energy on the N content. A band gap reduction by as much as 180 meV per mole percent of N has been observed in the low N composition range [8,9,10,11,12,13]. The strong effect of the N content on the electronic structure and the energy band gap have made GaAs based dilute nitrides important materials for a variety of applications, including long wavelength optoelectronic devices [14,15], high efficiency tandem [16,17] and intermediate band solar cells [18,19,20]. Although, most of the initial work has been focused on the GaAs based HMA it has been also shown that similar modifications of the electronic band structure is observed in other group III-V dilute nitrides including InN_xP_{1-x}, GaN_xP_{1-x}, GaN_xSb_{1-x}. [21,22,23,24,25,26] Also, comparable or even larger band gap reductions were observed in materials like $GaAs_{1-x}Bi_x$ [27,28], GaN-rich $GaN_{1-x}As_x$ [29] in which electronegative anions are partially replaced by more metallic atoms. Similarly, a large variety of group II-VI based HMAs have been studied including dilute oxides e.g. ZnO_xSe_{1-x} [30] and ZnO_xTe_{1-x} [31,32,33,34] where a small portion of metallic Se or Te is replaced with electronegative O, or dilute selenide $ZnSe_xO_{1-x}$ [35] or tellurides $ZnTe_xO_{1-x}$ [36] in which a fraction of O anions is replaced with Se or Te, respectively.

The unusually strong dependence of the fundamental gap on the N content in the group III-N-V alloys has been the subject of many theoretical investigations [8,13,37,38]. Calculations based on "*ab intio*" methods faced a difficulty with properly treating the dilute alloy limit as they required large size of supercells. Also such calculations were not capable of accurately determining the dispersion relations at the band edges. Inspired by the observed splitting of the conduction band of GaInNAs alloys a phenomenological model of the electronic band structure has been proposed [10]. The model considers repulsive interaction between the localized level of the minority element (N) and the extended states of the majority semiconductor phase (GaInAs). This band anticrossing model (BAC) [5,6,7,10] has been successful in explaining the experimentally observed electronic band structure of the dilute As-rich $GaN_{1-x}As_x$ alloys. The salient feature of the model i.e. splitting of the conduction band into two nonparabolic subbands $E_-(k)$ and $E_+(k)$ have been confirmed by measurements of the pressure dependence of the photo-modulated reflectance [10]. The downward shift of the lower subband (E_-) is responsible for the observed large reduction of the fundamental band gap.

The large difference in the size and electronegativity of the constituent atoms severely restricts solubility limits and the attainable composition range of HMAs. Most of the alloys were only studied in a dilute composition limit. Recent advances in understanding of the semiconductor synthesis processes allowed growth of thin films of HMAs under non-equilibrium conditions. Thus reducing the growth temperature allowed synthesis of group III-N-V HMAs over almost the entire composition range. The unusual evolution of the band gap and the conduction and valence band energies generated interest in potential applications of these HMAs for solar power conversion applications [39]. This review focuses on the GaN_xSb_{1-x} HMA which has been suggested as a potential material for solar driven water dissociation [40,41]. However it should be emphasized that the BAC model of the electronic band structure developed for the full composition of GaN_xSb_{1-x} is general and is applicable to any HMA. The paper is organized as follows. In the second chapter we introduce and discuss key general aspects of the BAC model that are applicable for HMAs in the entire composition range. Then the general aspects of the low temperature molecular beam epitaxy (LT-MBE) technique is described. In particular, properties of LT-MBE grown $GaN_{1-x}As_x$ HMA over the entire composition range are discussed as an example. Chapter 4 is devoted to discussion of the growth and various properties of GaN_{1-}

$_x$Sb$_x$ HMA. Finally, the potential of GaN$_{1-x}$As$_x$ HMA as a viable photoelectrode for PEC water splitting applications is discussed in Chapter 5.

2. **Band Anticrossing (BAC) Model for HMAs**

Well matched semiconductor alloys (such as In$_x$Ga$_{1-x}$As and Al$_x$Ga$_{1-x}$As) have been extensively studied and are relatively easy to synthesize in the whole composition range. In contrast, synthesis of highly mismatched alloys is much more difficult and, in many instances there are severe solubility limits for these materials. However, following the original success in synthesis of GaN$_x$As$_{1-x}$ with a few % of N, new methods have been developed to synthesize a large variety of HMAs [22,31,32,42].
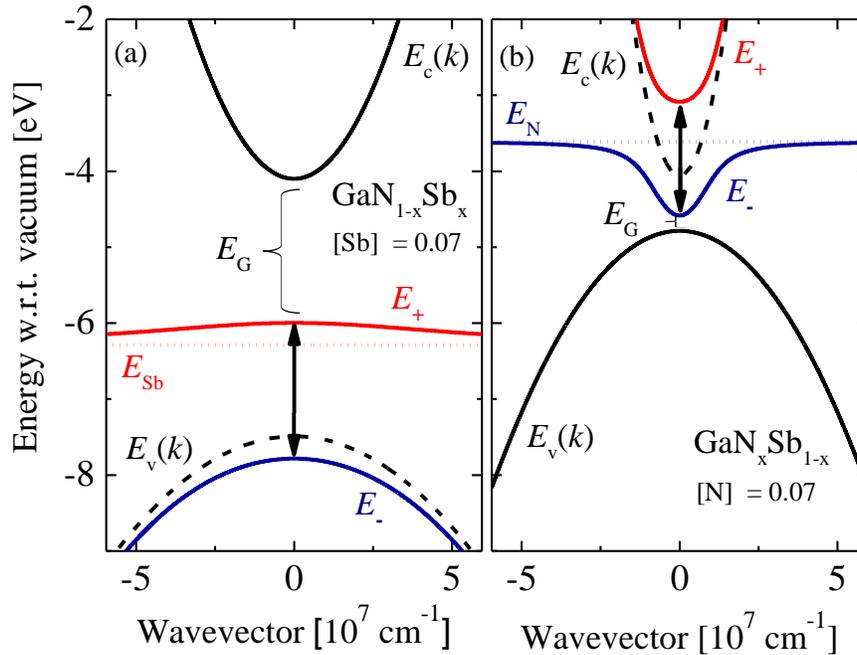

Fig. 1. Band splitting of (a) the valence band in GaN due to the localized Sb level and of (b) the conduction band in GaSb due to the localized N level. The arrows indicate the splitting of the band into two sub-bands. The bracket indicates the band gap of the dilute alloys. The black broken lines represent the original GaN valence band in (a) and the GaSb conduction band in (b).

The band anticrossing (BAC) model has been developed to calculate energy band structure in a system of extended band states interacting with highly localized states. In the first studied case of a HMA, host metallic As atoms were partially replaced with more electronegative N to form GaN$_x$As$_{1-x}$ alloys [10]. Substitutional N atoms produce highly localized states in the conduction band of the GaAs matrix. The repulsive, anticrossing interaction of these localized states with the extended, conduction band states leads to a drastic modification of the electronic band structure close to the conduction band edge (CBE). The interaction splits the conduction band into two subbands (E_+ and E_-). In the coherent potential approximation for spin independent interaction the dispersion relations for the two subbands are given by simple expressions obtained from a quantum mechanical solution of two sets of interacting states [5]. It has been shown that the BAC model applies to all group III-V dilute nitrides [6,7,10,21,22,24] as

well as group II-VI dilute oxides [30,31,32,33,34] or any HMA in which metallic atoms are partially substituted with more electronegative atoms [43]. It provides a description of the conduction band structure for the cases with localized levels in the band as well as with localized levels located in the band gap close to the CBE of the host material. For the specific case Sb-rich GaN$_x$Sb$_{1-x}$ the dispersion relation for the two CBE subbands are given by [10]:

$$E_\pm = \tfrac{1}{2}\{ (E_C(k) + E_N) \pm \sqrt{(E_C(k) - E_N)^2 + 4C_N^2(1 - x)}\}, \qquad (2)$$

where $E_C(k)$ is the CBE dispersion of the GaSb and E_N the energy of localized N derived states. The coupling parameter C_N describes the interaction between the two states, and x is the N content.

In the opposite case, a partial substitution of electronegative atoms with more metallic atoms leads to the formation of localized states in the valence band or in the band gap close to the VBE. For example, partial replacement of N with As or Sb in the GaN matrix leads to formation of a localized state at about 0.8 or 1.2 eV above the VBE, respectively. As both the extended valence band and the substitutional As or Sb states have p-symmetry the BAC interaction is more complicated, with the band structure of the VBE described by solutions of a 12x12 $k \cdot p$ matrix [29]. The problem can be simplified by ignoring spin-effects and separating the resulting 6x6 problem into three 2x2 problems. Thus for the example of N-rich GaNSb the dispersion relation of the two sub-bands can be described as [6,44]:

$$E_\pm = \tfrac{1}{2}\left\{ (E_V(k) + E_{Sb}) \pm \sqrt{(E_V(k) - E_{Sb})^2 + 4C_{Sb}^2 x}\right\}, \qquad (3)$$

where $E_V(k)$ denotes the valence band dispersion and E$_{Sb}$ the energy of localized Sb derived states. The coupling parameter C_{Sb} describes the interaction between the two states. Examples of the CBE and VBE splitting in Sb-rich and N-rich alloys are shown in Fig. 1. The N level is at E$_N$ = 0.45 eV above the CBE of GaSb, the Sb level at E$_{Sb}$= 1.2 eV above the VBE of GaN. As can be seen in the figure, dilute concentrations of either of the substitutional elements causes the band gap of the alloys to decrease substantially.

2.1 BAC of HMAs for the entire composition range

In its simple form the BAC model is applicable only to dilute alloys in which the effects of the minority constituents can be treated as a small perturbation. However a good description of the electronic structures of HMAs across the entire composition range requires modification of the BAC model. In the first approximation it was proposed that the BAC model can be extended to the whole composition range by compositional weighting of the BAC results obtained in the dilute limits [29]. This approach has been developed for GaN$_{1-x}$As$_x$ [39]. As will be discussed later in section 3.3 in a study of the composition dependence of the bandgap of GaN$_{1-x}$As$_x$ over the entire composition range at dilute composition limits (dilute-N GaAs and dilute-As GaN), the

calculated band gap is in a reasonably good agreement with the experimentally determined optical band gaps [11,29,39] (Fig. 8(b)).

The compositionally weighted BAC model has been also used to calculate the band gap of the group II-IV HMAs including $ZnO_{1-x}S_x$ [45], $ZnO_{1-x}Se_x$ [35], and $ZnO_{1-x}Te_x$ [36]. In general the BAC model describes the electronic band structure for dilute group II-IV and III-V HMAs very well. However for alloys with mid-range compositions, the model tends to overestimate the band gap reductions.

2.2 The modified BAC model

The BAC model provides an accurate description of the electronic band structure of dilute group III-V and II-VI HMAs. However the extension of the model to the whole composition range by compositional weighting of the BAC models for the conduction and the valence band is not well justified. The main deficiencies of the compositionally weighted BAC model are that it ignores direct dependence of the coupling parameter on composition and that it uses the end-point CBE and VBE energies as the host matrix values. In order to address these deficiencies we have proposed a new hybrid BAC model [46] in which the composition dependence of CBE and VBE is separated into two contributions: the band edge shifts originating from a change of crystalline potential in the VCA and from a BAC interaction between localized states and the virtual crystal as a host matrix. This allows the BAC interactions to be treated as perturbations. In the VCA the VBE and CBE for $GaN_{1-x}Sb_x$, are given by linear interpolation between the end point compounds:

$$E_V(x, k = 0) = (1\text{-}x)E_{V,GaN} + xE_{V,GaSb} \tag{4}$$

$$E_C(x, k = 0) = (1 - x)E_{C,GaN} + xE_{C,GaSb}, \tag{5}$$

$E_{V,GaN}$ and $E_{V,GaSb}$ denotes the VBEs, and $E_{C,GaN}$ and $E_{C,GaSb}$ of the CBEs of GaN and GaSb, respectively.

Also in the VCA, the lattice site potential for the $GaN_{1-x}Sb_x$ alloy is given by the average potential

$$V_{vc}(x) = (1\text{-}x)V_N + xV_{Sb}, \tag{6}$$

where V_N and V_{Sb} are the potentials of the lattice sites occupied by N and Sb atoms, respectively. In this approximation the coupling parameter for the N atom substituting a virtual crystal site is given by the matrix element

$$C_N(x) = \langle f|V_N(1 - x) + xV_{Sb} - V_N|f\rangle = xC_{No}, \tag{7}$$

where $\langle f|$ is the Bloch wavefunction obtained in the VCA and $C_{No} = \langle f|V_{Sb} - V_N|f\rangle$ is the coupling constant in the dilute N limit. In a similar manner it can be shown that the composition dependence of the coupling constant for the BAC interaction between the valence band and the

localized Sb level is given by $C_{Sb}(x) = (1 - x)C_{Sbo}$ where C_{Sbo} is the coupling constant in the dilute Sb limit.

Figure 2 shows the electronic band structure close to the VBE and CBE for GaN$_{1-x}$Sb$_x$ with several different alloy compositions calculated using the modified BAC model. The arrows in the figure illustrate the linear dependence of the VCA matrix band edges on the Sb concentration. The band gap is given as the energy difference between the E_-^C and the E_+^V bands. Here, for illustrative purposes, we have used a simplified valence band structure by ignoring spin orbit splitting of the valence band and the localized Sb level. However as we will discussed later the spin orbit splitting has to be included in the fitting of the optical absorption curves for the accurate determination of the composition dependent band gap. As can be seen in the figure, the drastic narrowing of the bandgap of GaN-rich GaN$_{1-x}$Sb$_x$ HMA arises primarily from the modification of the valence band due to the BAC interaction between the GaN valence band with the Sb localized levels. On the other hand, the BAC interaction between the conduction band of GaSb and the localized N levels has a dominant effect on the band gap in the GaSb-rich alloys.
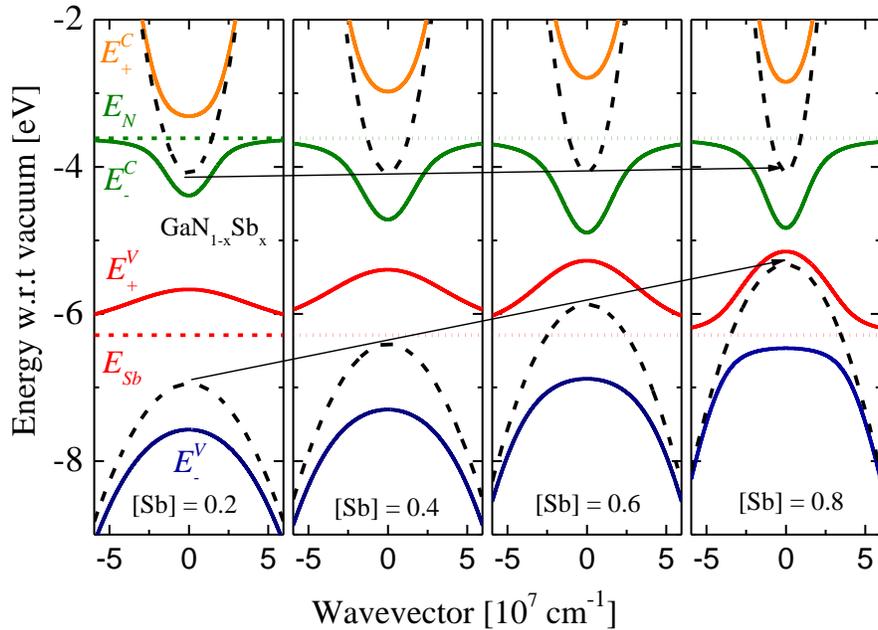

Fig. 2. The GaN$_{1-x}$Sb$_x$ dispersion relations calculated using the modified BAC model. The dashed black lines represent the valence and the conduction band edges of the matrix using the VCA, the arrows shows the linear change with increased Sb content. The band gap is defined as the difference in energy of the E_-^C and the E_+^V band.

3. Low temperature MBE growth of N-rich HMAs

3.1. Low temperature MBE

Under most conventional growth conditions, GaN crystallizes in the wurtzite structure, which has a hexagonal symmetry. High quality GaN for device applications are typically grown by metal organic chemical vapor phase deposition (MOCVD), hydride vapor phase epitaxy (HVPE), and molecular beam epitaxy (MBE). Of these methods, MBE is inherently slower, but

affords advantages of atomic and chemical precision. MBE allows the formation of metastable phases of GaN, and also allows lower temperature growth, whereas the CVD processes require high growth temperatures exceeding 1000°C to crack the ammonia molecules. The first few decades of GaN research was hindered by the lack of suitable bulk GaN substrates onto which lattice-matched group III-nitride films could be grown. GaN has been grown on non-lattice-matched and non-isomorphic sapphire [47], SiC [48], GaAs [49] and Si [49,50]. Crystalline GaN templates now exist [51,52,53], but even today devices fabricated from GaN based compounds are grown on non-native substrates [54,55]. Examples include commercially available LEDs, produced from GaN or InGaN grown on SiC or sapphire, and GaN power transistors, which use sapphire substrates.

High temperatures of 800-1000°C were traditionally and are currently used for GaN growth in both MBE and MOCVD to mitigate the energy barriers to precursor adsorption and surface adatom migration [56]. Such high growth temperatures, however, prevent the incorporation of substantial amounts of highly mismatched isovalent elements in the crystal lattice of GaN. For the synthesis of materials with constituents having drastically different chemical or physical properties at compositions or structures far exceeding their thermodynamic solubility limits, extreme nonequilibrium techniques are required. The atomic diffusion length in these nonequilibrium processes has to be long enough to form crystalline lattices with uniform compositions, but short enough to avoid equilibrium phase segregation. This has been recently demonstrated in the growth of single phase ferromagnetic $Ga_{1-x}Mn_xAs$ with Mn concentration as high as 16% using the low temperature molecular beam epitaxy (LT-MBE) technique [57,58]. Figure 3 shows a schematic "phase diagram" relating the MBE growth temperature with the different phases observed in $Ga_{1-x}Mn_xAs$ alloys [57].
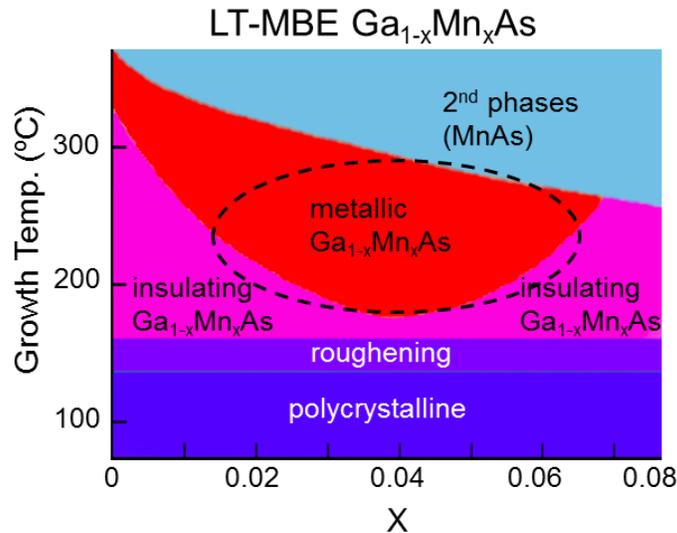

Fig. 3 A schematic relating different crystalline phase of $Ga_{1-x}Mn_xAs$ with MBE growth temperature. Adapted from Ohno et al. [57]

It has been shown previously that MBE growth of GaAs at low temperature (LT-MBE) in the range of 200-350°C resulted in materials with many interesting properties such as a high

defect concentration and high electrical resistivity. LT-MBE-GaAs layers grown at substrate temperatures in the range of 200- 250°C are good quality single crystals with > 1 at. % excess arsenic [59,60]. Electron paramagnetic resonance measurements on LT-MBE-GaAs layers showed that these layers have ~$5x10^{18}$cm^{-3} arsenic antisite defects [59]. The short lifetime allows for ultrafast switching, with mobilities that are still sufficient for good switch responsivity. This material found applications as buffer layers to eliminate the backgating effect for GaAs FET's [61], as ultrafast photoconductive switches [62], and in quantum cascade lasers for THz spectroscopy applications [63].

3.2 LT-MBE grown GaN

Because of the technological potential of LT-MBE GaAs, a lot of work has been performed on understanding the defects in this material [59,60,61,64,65,66,67]. In contrast only a few reports have been published on gallium nitride grown at low temperature [68,69]. Most of these previous studies focused on the structural properties of GaN synthesized at low temperatures (<300°C) by radio frequency sputtering. In MBE high quality GaN thin films for optoelectronic applications are typically grown at a growth temperature ≥800°C. Recently as part of our investigation on the low temperature synthesis of highly mismatched GaN$_{1-x}$As$_x$ [39] and GaN$_{1-x}$Sb$_x$ [41,70] alloys, we explored LT-MBE synthesis of GaN thin films grown at temperatures ranging from ~80 to 500°C under a wide range of Ga:N flux ratios [71].

It is now well established that there are three main regimes for plasma assisted (PA)-MBE growth of GaN; N-rich growth when the active nitrogen flux is larger than the Ga-flux, Ga-rich growth when the active nitrogen flux is less than the Ga-flux, and extremely Ga-rich growth when the active nitrogen flux is much less than the Ga-flux. In the latter case Ga droplets are formed on the film surface. The most common approach for determining the conditions at which the Ga- and N-fluxes are the same is to fix the N-growth conditions and to grow a series of films for equal amounts of time, each one with increasing Ga-flux, and then to measure the resulting film thicknesses. As long as there is an excess of N, the GaN growth rate is proportional to the Ga-flux. This produces films with increasing thicknesses up the point where the Ga and N fluxes are equal. For higher Ga-fluxes, GaN cannot form resulting in metallic Ga coverage. This is obviously a time-consuming method and alternative approaches such as analysis of reflection high-energy electron diffraction (RHEED) patterns have also been employed. The latter, however, requires growth at the high temperatures that usually employed for growth of GaN, and therefore would not be an easily amenable technique for the low growth temperatures used for the HMAs.

To quickly determine the fluxes at temperatures required for HMA growth we have employed a new *in-situ* Auger electron probe that allows chemical analysis during deposition [72]. In these experiments we fix the N flux and program a linear Ga-flux ramp, while observing the emitted Auger electrons from nitrogen that are excited by the RHEED electron gun. The intensity of the signal is proportional to the concentration of nitrogen within the escape depth of the material which is on the monolayer scale. Thus plotting the N Auger electron signal as a function of time shows an initial rapid increase representing the formation of a GaN film. Once the film thickness exceeds the escape depth the signal saturates at a constant level while the Ga-flux is less than the N-flux. Right after the Ga-flux reaches the point where it is equal to the N-flux, the N-Auger signal starts dropping. This is because the surface now exhibits an

accumulation of Ga-droplets which prevent an increasing fraction of the N-Auger electrons from escaping.

The time for the experiment is a trade-off between Ga-cell control and sampling rate of the probe. We have found that a two-hour ramp gives reliable data for determining the 1:1 transition point. This is a marked improvement over growth and thickness analysis of multiple samples, which would take several days. In our current study, a constant N flux corresponding to a total N beam equivalent pressure (BEP) ~1.5 10^{-5} Torr, RF power 200W was maintained. We have determined that N-rich and Ga-rich conditions correspond to Ga BEP $<2 \times 10^{-7}$ and $>2 \times 10^{-7}$ Torr, respectively.

We found that reduction of the growth temperature to 200°C results in epitaxial GaN films with a high density of dislocations and small size (30-50 nm) columns. At an even lower growth temperature of 80°C, GaN films still exhibit a polycrystalline columnar morphology with high c-axis orientation and average column widths varying from 10 nm near the sapphire interface to 14 nm near the surface. This can be attributed to the high ionicity of GaN that prevents the material from becoming amorphous. From X-ray diffraction studies we estimated that at T_g~80°C the c-axis lattice parameter c increases by 0.44%. The reduction of the diffraction peak intensity and an increase in the peak width also suggest that the crystallinity of the films decreases strongly as the T_g decreases.   It is estimated that the grain size decreases from 100 nm (T_g~540°C) to 30 nm (T_g~80°C). Fig. 4 shows a cross sectional TEM from a GaN samples grown at 80°C under N-rich (Ga BEP~1.6x10^{-7} Torr) conditions. Despite the extremely low growth temperature, the sample has a polycrystalline, columnar morphology. Similarly films grown under Ga-rich conditions with much higher Ga BEP exhibit very similar microstructures (not shown). The selected area diffraction (SAD) pattern shows clear polycrystalline rings, confirming the XRD results. The high-resolution image in Fig. 4 show that most of the grains are aligned with the c-plane normal or at a slight angle to the growth direction.
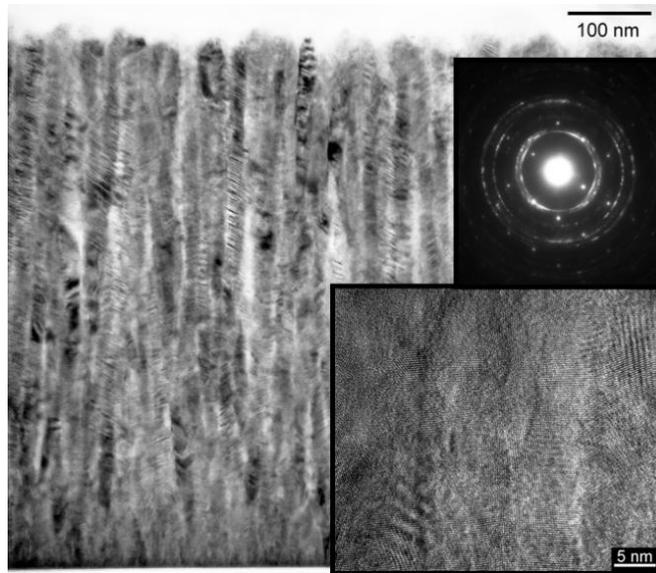

Fig. 4 TEM images of N-rich (Ga BEP~1.6x10^{-7} Torr) GaN thin films grown at 80°C. Reprinted with permission from reference [71]. Copyright 2015 IOP Publishing Ltd.

The optical absorption properties of GaN films grown at low temperature under N-rich condition are similar to normal GaN. The LT-MBE GaN films grown under Ga-rich (Ga BEP $>2\text{x}10^{-7}$ Torr) conditions are found to be conducting with resistivity in the range of 10^{-1}-10^{-3} Ω-cm. The charge transport was determined by thermopower measurements to be dominated by holes. However it was also found that for the constant Ga BEP of $2.2\text{x}10^{-7}$ Torr there is a change of the thermopower type from p to n for $T_g > 350^\circ$C.

The absorption coefficient α of GaN films was determined from transmission and reflection measurements in the wavelength range of 200-2600 nm. Fig. 5(a) shows α for GaN films grown at 80°C under different Ga fluxes. A monotonic increase in low energy absorption is observed when the Ga BEP increases during growth. Strong absorption at energies as low as 1 eV is observed for samples grown under very high Ga BEP ($>2.2\text{x}10^{-7}$ Torr). The high absorption coefficient ($\alpha>10^4$ cm^{-1}) at low energy for Ga-rich grown films combined with the observations of extremely low carrier mobility and growth conditions dependent polarity of the thermopower indicate the presence of a large density of native defect states in the band gap.
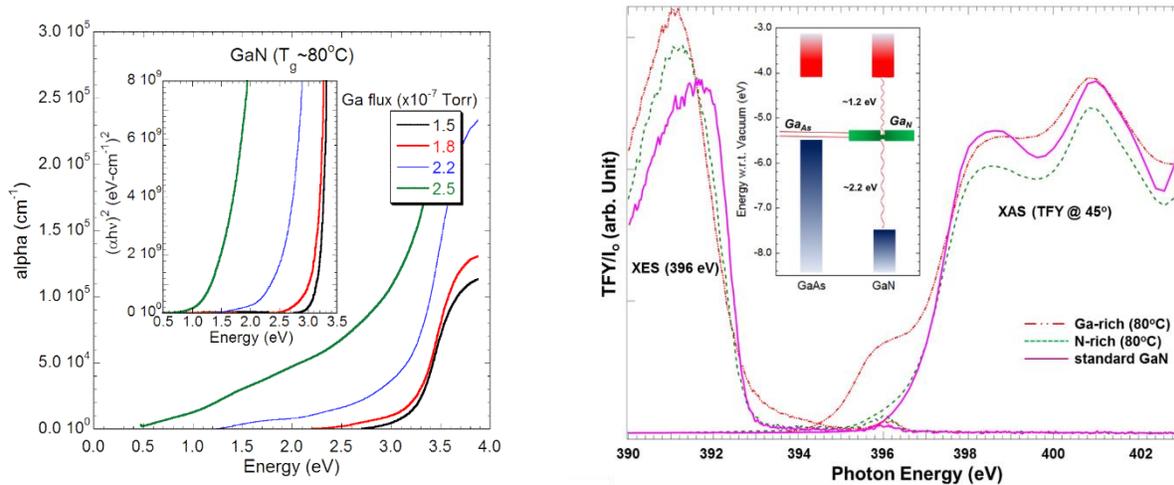

Fig. 5(a) Absorption coefficient, α for GaN films with increasing Ga BEP content grown at 80°C under different Ga flux. (b) The nitrogen K-edge XES (left side) and total fluorescence yield XAS (right side) of GaN films grown at 80°C with different Ga BEP and a standard GaN thin film grown by plasma assisted MBE at ~800°C. The threshold-excited elastic emission peak near 396 eV was used to align the XES spectra to the XAS. The inset is a schematic diagram showing the possible location of the Ga antisites in GaAs and GaN. Reprinted with permission from reference [71]. Copyright 2015 IOP Publishing Ltd.

Fig. 5(b) shows soft X-ray absorption and emission spectra for LT-GaN samples grown with different Ga fluxes. The appearance of a near zero gap for the Ga-rich LT-GaN film suggests that there is a very small energy separating occupied from unoccupied states. This is consistent with the presence of a large concentration of Ga_N defects, forming a partially occupied band located at ~1.2 eV below the CBM of GaN and with the strong sub-bandgap optical absorption shown in Fig. 6(a). The XAS and XES results then correspond to the partial density of states of these Ga_N defect states hybridized with N 2p states. The p-type conductivity observed in the Ga-rich samples can also be explained by a charge transport within this partially filled Ga_N

12

defect band. A schematic diagram showing the location of the Ga antisites in GaAs and GaN is shown in the inset Fig. 5(b). The p-type conductivity of this defect band due to low temperature growth can be exploited for the fabrication of low resistivity p-type ohmic contacts on GaN devices.

3.3 LT-MBE grown GaN$_{1-x}$As$_x$ over the entire composition range

In contrast to the very extensively studied As-rich GaNAs alloys much less work has been devoted to HMAs on the N-rich side of this alloy system. It was found that GaN doped with As at low, impurity-like levels show a characteristic blue emission at room temperature. At higher As doping levels an abrupt decrease in the band gap of resulting GaN$_{1-x}$As$_x$ alloys was observed [73,74,75,]. Wu et al. [29] investigated the BAC in N-rich and As-rich GaNAs alloys with a limited range of composition and interpolated the composition dependence of the band gap of GaN$_{1-x}$As$_x$ alloys over the entire composition. The calculations predict a minimum band gap of 0.7 eV at x~0.8. This is in a stark contrast to the composition dependence of the band gap predicted by the VCA and the quadratic fitting (Equation (1)) with a large bowing parameter b=16.2 eV. However, neither of these predictions could be tested as there had been no experimental data for alloys in the middle 85% of the alloy composition.

Using highly non-equilibrium LT-MBE with growth temperatures as low as 200°C we have synthesized GaN$_{1-x}$As$_x$ across the entire composition range [39,76,77]. The resulting alloys are amorphous in the intermediate composition range (0.10 $<x<$ 0.75), with the transition between crystalline to amorphous structure depending on the growth substrate. For example, the N-rich alloy remains in the wurtzite structure for higher As concentrations when grown on sapphire instead of glass [77] and the As-rich alloy remains in the zinc blende structure for higher N concentrations when grown on silicon. We found that epitaxy of GaN$_{1-x}$As$_x$ under Ga-rich growth conditions at relatively high temperatures of ~600°C results in phase separation into GaN:As and GaAs:N for x>0.02. As the growth temperature is reduced from ~600 to 100°C, along with the increase in the As incorporation from x~0.02 to 0.7, the structure of the GaN$_{1-x}$As$_x$ film transforms from single crystalline to polycrystalline (~500°C) to amorphous (<410°C).

Figure 6(a) shows a series of SAD from alloys with increasing As content as a result of decreasing growth temperature from 550 to 100°C. The SAD results unambiguously illustrate that the GaN$_{1-x}$As$_x$ alloys go from single crystalline spot pattern (T$_g$=550°C) to polycrystalline ring pattern (400°C<T$_g$<500°C) to amorphous diffuse ring pattern (T$_g$<400°C; x>0.2). The diffuse ring patterns for GaN$_{1-x}$As$_x$ alloys with x in the range of ~0.2 to 0.75 confirm that these alloys are amorphous with no observable nanoscale secondary phases. We also found that at the same growth temperature, the As content in the amorphous film increases with the As flux during growth. This is illustrated in Fig. 6(a) by the SAD patterns from two amorphous samples grown at 210°C: the sample with 45% As was grown with ~6X higher As flux as the sample with 27% As. The SAD pattern for the As-rich GaN$_{1-x}$As$_x$ film with x= 0.86 grown at ~200°C is also shown in Fig. 6(a). The ring pattern for this sample is consistent with the XRD result that cubic polycrystalline phase of GaN$_{1-x}$As$_x$ was formed for As-rich alloys [39].

TEM micrograph of the crystalline 2% As film (not shown) reveals a columnar crystalline film with high density of planar defects. These columns are misoriented with respect to each other; therefore dislocations need to form to accommodate this misorientation. Fig. 6(b) is a high resolution micrograph of an As rich amorphous film (x=0.45; T_g=210°C) confirming the amorphous nature of this film with no observable composition segregation. We also note that the range of amorphous phase is dependent on the substrate used. While on sapphire substrates, the alloys are amorphous in the composition range of 0.17<x<0.75 and crystalline outside this region [39]. For the films grown on Pyrex substrates, the composition range for amorphous alloys extends to x~0.1 [77]. The amorphous nature of these films were further confirmed by extended X-ray absorption fine structure measurements [78].
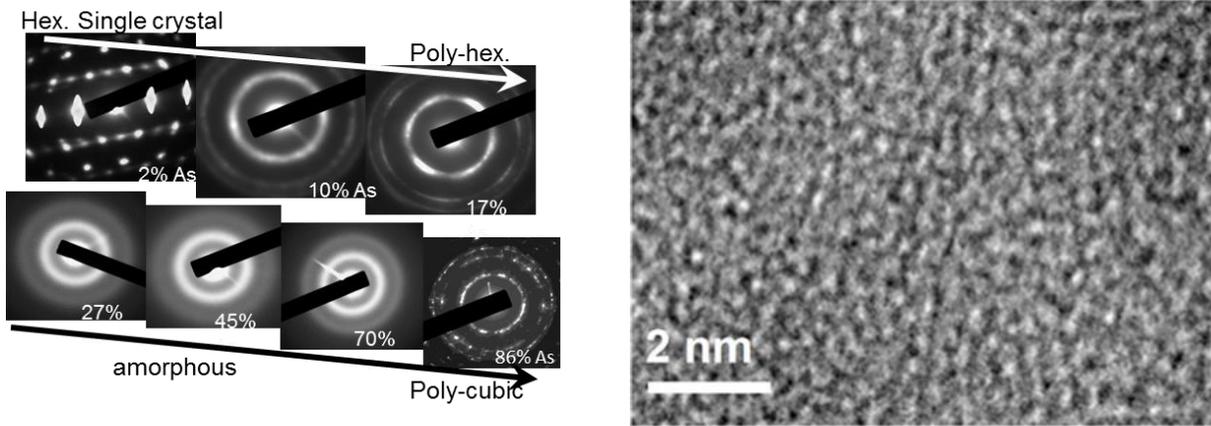

Fig. 6 (a) A series of selective area diffraction patterns (SAD) patterns from GaN$_{1-x}$As$_x$ alloys with increasing As content as a result of decreasing growth temperature from 550 to 100°C. (b) A cross-sectional TEM micrograph of an amorphous GaN$_{1-x}$As$_x$ film (x=0.45; T_g=210°C). Reprinted with permission from reference [39]. Copyright 2009 AIP Publishing LLC.

The E_g of GaN$_{1-x}$As$_x$ changes monotonically across the crystalline − amorphous boundary and as the amorphous phase composition is varied, in qualitative agreement with the band anti-crossing model for HMAs. Taking into account both crystalline and amorphous phases, the band gap of the GaN$_{1-x}$As$_x$ alloy system goes from 0.8 eV to 3.4 eV. Fig. 7(a) shows a series of photoreflectance (PR) spectra from amorphous GaN$_{1-x}$As$_x$ samples with x=0.15-0.45. A gradual decrease of the GaN$_{1-x}$As$_x$ band gap as x increases is clearly shown. These band gap values are further confirmed by optical absorption measurements that showed sharp absorption edges for all the amorphous films with absorption coefficient ~1x10^5 cm^{-1} at ~0.5 eV above the band gap. The inset of Fig. 7(a) compares the PR and absorption spectra from a GaN$_{0.76}$As$_{0.24}$ sample. The clear observation of the PR signal indicates an extended rather than localized nature of the band edge states. This is also consistent with an abrupt onset of the absorption edges and an absence of defused absorption tails that are typical in amorphous silicon.

The band gap as measured by PR on the GaN$_{1-x}$As$_x$ films grown on Pyrex are shown in Fig. 7(b) together with data taken from films grown on sapphire. Band gap values for dilute alloys (As-rich [11] and N-rich [29] GaNAs) from the literature are also presented. The composition dependence of the band gap of GaN$_{1-x}$As$_x$ alloys over the entire composition range shown in Fig. 7(b) was calculated by a weighted interpolation of the BAC calculated curves for

14

N-rich and As-rich dilute alloys [29] as discussed in section 2.1. Comparing our experimental data (both on sapphire and Pyrex) directly with the BAC model we notice that the band gap values for the crystalline and amorphous $GaN_{1-x}As_x$ alloys are in good agreement with the BAC model. The results suggest that for this composition range the amorphous $GaN_{1-x}As_x$ alloys have short-range ordering that resembles random crystalline $GaN_{1-x}As_x$ alloys. Moreover, soft X-ray absorption (XAS) and emission (XES) measurements revealed that this reduction in the bandgap indeed arises from the VB change due to valence N states hybridizing with an As impurity level just above the GaN valence band maximum (VBM). This observation is in excellent agreement with predictions of the BAC model in this dilute doping regime [39].
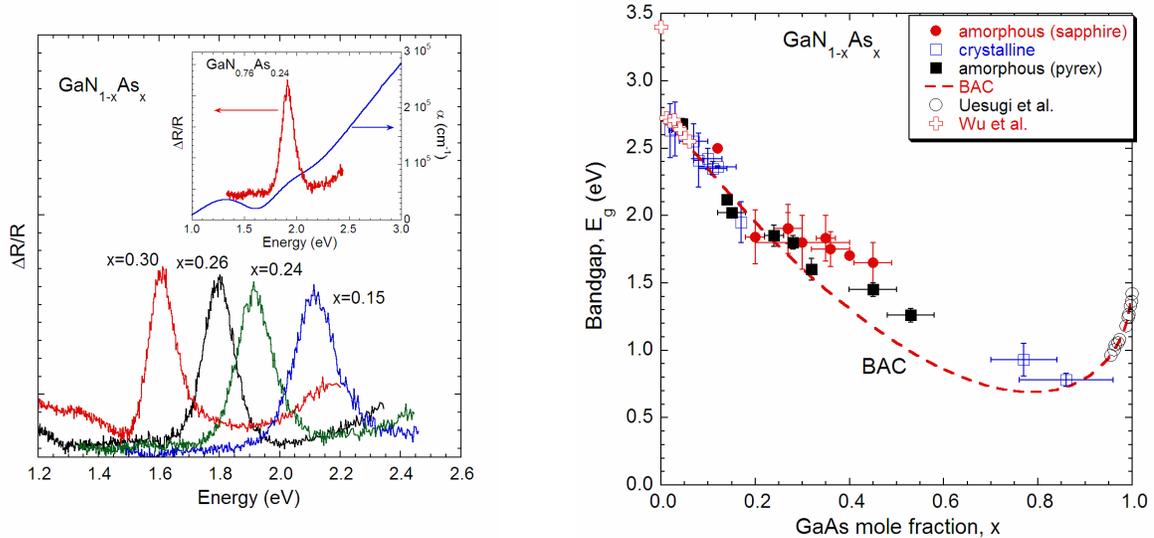

Figure 7 (a) Photomodulated reflectance (PR) spectra from $GaN_{1-x}As_x$ thin films on a Pyrex substrate with x in the range of 0.15 to 0.45. The inset shows a comparison between the PR and absorption spectra from a $GaN_{0.76}As_{0.24}$ sample. (b) Band gap energy as a function of As content x for $GaN_{1-x}As_x$ alloys. Band gap values from both crystalline and amorphous alloys grown on sapphire and Pyrex are shown together with results from reported crystalline As-rich and N-rich $GaN_{1-x}As_x$ alloys (from references 3,11 and 29). Calculated composition dependence of the band gap of $GaN_{1-x}As_x$ alloys based on the BAC is also shown. Reprinted with permission from reference [77]. Copyright 2010 AIP Publishing LLC.

Due to the low growth temperature of 200-320°C and the amorphous structure, these $GaN_{1-x}As_x$ films can be grown on low cost glass substrates instead of expensive single crystal substrates. Despite the highly non-equilibrium composition of these alloys, they are remarkably stable for short excursions beyond 700°C prior to phase segregation [79]. The thermal stability of these alloys is important for functionalization due to various high temperature semiconductor processing techniques (e.g. dielectric deposition). Furthermore, both p-type and n-type doping of a partially amorphous $GaN_{1-x}As_x$ (x~0.55-0.65) have been demonstrated [80,81]. We observed that the room temperature p-type conductivity of $GaN_{1-x}As_x$ increased monotonically with increasing of Mg content, up to a maximum value of about 55 S/cm for 8 atomic % Mg content [80]. We have found that achieving of the p-type doping of $GaN_{1-x}As_x$, requires growth under Ga-rich conditions. These conditions result in the formation of As-rich crystalline GaAs:N inclusions inside the amorphous GaNAs matrix, which can be observed in the X-ray diffraction

(XRD) and transmission electron microscopy (TEM). Recently we have also successfully identified the range of the growth parameters for a reproducible and uniform Te incorporation in amorphous $GaN_{1-x}As_x$:Te layers with x close to 0.6 and a maximum Te concentration of $9x10^{20}cm^{-3}$[81]. Te incorporation resulted in n-type doping with film resistivities below10 Ω-cm, electron concentration in mid $10^{19}cm^{-3}$ and electron mobilities of ~1cm^2/Vs. The ability to control the electrical properties of these alloys that exhibit a wide bandgap range of 0.8-3.4 eV can lead to exciting applications in electronics and photovoltaics.

4   LT-MBE GaN$_{1-x}$Sb$_x$ HMAs

For photoelectrochemical water-splitting application, an ideal photoelectrode must meet three criteria: corrosion stability, a band gap between 1.8 and 2 eV to produce sufficient over-potential to drive the water-splitting reactions while still absorbing a significant fraction of the solar spectrum, and band edges straddling the hydrogen and oxygen redox potentials for spontaneous water splitting [82,83]. Since the anion mismatch is even larger between Sb and N, BAC calculations on the electronic band structure of the $GaN_{1-x}Sb_x$ alloys predict that less than 6% of Sb is needed to achieve an alloy with a bandgap ~2.2 eV with the conduction band minimum (CBM) and the valence band maximum (VBM) still straddling the water redox potentials. Hence $GaN_{1-x}Sb_x$ HMAs could be suitable as photoelectrodes for photoelectrochemical water splitting applications [40]. Although GaSbN dilute nitride films have been studied in the last decade, there is little to nothing known about the growth of $GaN_{1-x}Sb_x$ alloys in the N-rich regime.

4.1 GaSb-rich dilute nitride HMA

It was recognized that addition of N to GaSb could potentially produce a direct bandgap material suitable for long-wave infrared detection [84,85,86,87,88,89,90]. By also alloying on the group III site with In, it could be possible to drastically reduce the bandgap while staying lattice matched to a GaSb substrate [89,86,90,91,92]. Such large band gap bowing has also been explained using the BAC model taking into account the modification of the conduction band of GaSb by the localized N states [87,88,90]. Using Fourier transform IR absorption measurements on GaNSb HMAs with N content in the range of 0.2 to 1.0%, Jefferson et al. demonstrated that the anticrossing coupling parameter was 2.6 eV with the N state at 0.78 eV above the valence band of GaSb [88].

Buckle et al. found that the apparent incorporation of N in GaSb was easily controlled with the substrate temperature and demonstrated incorporation up to 1.75% [93]. In the same way, Wang et al. reported the incorporation of up to 1.4% N in GaSb and verified the reduction in bandgap using optical absorption and photoluminescence [84]. Unfortunately, the lower substrate temperature growth process also resulted in a dramatic degradation in the crystalline as well as electro-optical qualities of the films. The unintentional background p-type carrier concentration increased from low 10^{15} cm^{-3} by several orders of magnitude. At the same time, the minority carrier lifetime of GaSb, which is not competitive to begin with at ~35 ns, degraded to the femto-second range. The degradation of the optical quality of these dilute alloys were believed to arise from non-radiative centers. It was speculated that these non-radiative centers are due to the presence of N-As and N-N split interstitials [94]. A recent study by Nair et al. correlating photolumescence intensities with X-ray diffraction and ion channeling measurements

on GaInSbN quantum wells confirmed the presence of these non-radiative centers due to non-substitutional N, possibly in the form of N clusters and split interstitials [86].

Most of these early experiments relied on X-ray diffraction for the determination of the concentration of N in the films. Based on the observation of text-book Pendelloesung fringes, the structural quality of the films was prematurely judged to be very high. The reduction of the bandgap with the X-ray derived N-concentration also indicated a well-behaved alloy system. Later, however, it became apparent that the total amount of N in all films produced in this way *was the same* within experimental errors. By examining the nitrogen content with chemical analysis methods that sample *all* atoms, irrespective of lattice position, such as secondary ion mass spectroscopy (SIMS) or Rutherford back scattering (RBS) it was determined that the substrate temperature only affected the group-V lattice site occupation of *some* of the nitrogen atoms. These atoms did reduce the bandgap following the BAC model, while the rest of the nitrogen was apparently optically inactive. These non-substitutional N were referred to as "dark nitrogen" [95].

The origin of the "dark nitrogen" was investigated using channeling nuclear reaction analysis and was consistent with interstitials or split interstitials defects [86]. This, however, relies on the assumption of a non-distorted homogeneous film. Using high-resolution transmission electron microcopy we have observed that the introduction of N in GaSb also produces an undulating layering that is not detected by X-ray diffraction. The incorporation of small amounts of N in the GaSb lattice is still not completely understood, but may hint at a common issue with the alloy. The contradictory XRD and chemical analysis results are mirrored in a perplexing way on the opposite composition end, where it is the chemical concentration measurements that correlate with the bandgap shift while the XRD results are sometimes unaffected.

Research in this material system, however, became less active after the discovery that the bandgap of InAsSb is small enough to achieve an optical gap in the 8-12 micron range, and which can be grown with very high quality [96,97]. Nevertheless, the dilute N GaSb(N) work revealed some intriguing growth and materials properties that may have general implications for alloying on GaN-rich end of the $GaN_{1-x}Sb_x$ composition spectrum.

4.2 GaN-rich $GaN_{1-x}Sb_x$ alloys

Although GaSbN dilute nitride films have been studied in the last decade there has been no report on the growth of $GaN_{1-x}Sb_x$ alloys in the N-rich regime. The alloys discussed in this paper were grown at the University of Nottingham (chamber 1) and the US Army Research Laboratory (chamber 2). Chamber 1 is a MOD-GEN II system with a HD-25 Oxford Applied Research RF activated plasma source to provide active nitrogen, and elemental Ga and Sb as group III and V sources. The surface reconstruction is monitored with RHEED. Prior to the growth of the $GaN_{1-x}Sb_x$ layers, the sapphire wafers were annealed at 700°C for 20 min. After annealing, the substrate was cooled down to the growth temperature over a 20 min period under a reduced active nitrogen flux and growth was initiated by simultaneous opening of the Ga and N shutters. The Sb shutter was opened after a 1 min delay in order to avoid the deposition of any Sb on the sapphire surface before GaN growth. The growth time was kept constant at 2 hr for all layers. Chamber 2 is a GEN II system with a Veeco Uni-bulb plasma source to provide active N,

elemental Ga and a Veeco valved cracker-sources for Sb. In both systems the uncoated sapphire substrate temperature was set by the thermocouple. The source and pumping arrangement in Chamber 2 produces significantly less atomic N; therefore growths are done at a much slower rate than used in Chamber 1.

4.2.1 Sb incorporation

Previously, we found that growth of $GaN_{1-x}As_x$ with x>0.02 under Ga-rich growth conditions and at relatively high temperatures of ~600°C results in phase separation into N-rich and As-rich phases [39]. Since Sb and N are even more mismatched in size and electronegativity than As and N, we expect that the incorporation of Sb in the N sublattice will be even more challenging. In order to incorporate substantial amounts of Sb into GaN we grew N-rich dilute Sb samples on (0001) sapphire substrates by plasma-assisted MBE in chamber 1 at thermocouple temperatures ranging from 80° to 600° C, significantly below the normal MBE GaN growth temperature of ~800°C.

The initial experiments included two series of Ga -rich (Ga BEP~2.2x10^{-7} Torr) and N-rich (Ga BEP~1.6x10^{-7} Torr) growth conditions grown in Chamber 1 at an extremely low temperature of 80°C under fixed Ga and N overpressures, but different Sb overpressures. A constant N flux (total N beam equivalent pressure (BEP) ~1.5 10^{-5} Torr with RF power 200W) was maintained for these series. In both series, there was a monotonic increase in Sb content with increasing Sb overpressure, as shown in Fig 8, where the composition is plotted as a function of the Sb/N beam equivalent pressure (BEP) ratio. The Ga-rich samples were grown at 0.27 μm/hr and the N rich samples were grown at 0.23 μm/hr.
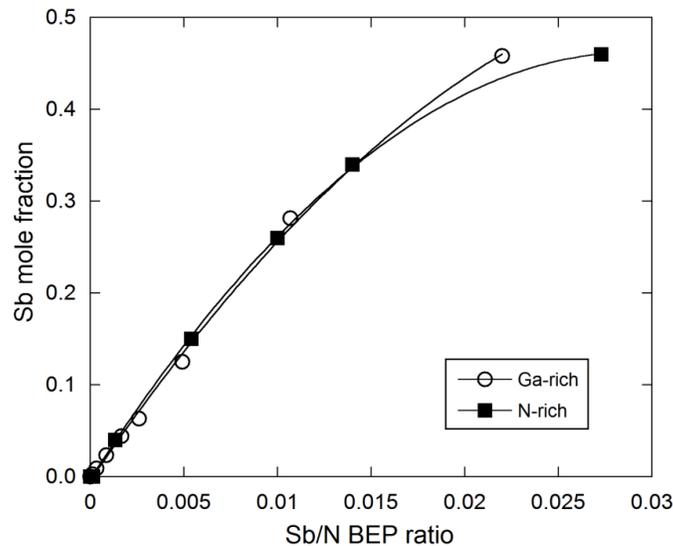

Fig. 8 Incorporation of Sb in GaNSb as a function of Sb flux for both Ga-rich and N-rich growth conditions at 80°C.

It is known that the group III growth rate affects the group V compositions in group III-V alloys with mixed group constituents. For instance, for other fixed conditions, the Sb incorporation into GaAsSb and InAsSb [98] increases by a non-negligible amount at the expense

of As as the cation flux increases. The interaction between Sb and N in relation to the Ga flux in our case is not yet known. For samples with lower Sb composition (<25%), the relationship between the Sb/N BEP ratio and the Sb composition appears to be linear and unaffected by the change in Ga flux. For Sb compositions above 35% it appears that the Ga-rich sample incorporates more Sb as a function of the BEP ratio. This is intuitive since the Sb should want to stick to the Ga-terminated surface, especially in a group V-deficient environment. We also noticed in prior InAsSb and GaAsSb experiments that for slow growth rates, it took a much larger change in the group V flux ratio to effect a significant change in the composition [98]. If the GaNSb HMAs could be grown faster, it would likely require a much smaller change in the Sb/N ratio to increase the Sb composition.

The incorporation of the Sb as a function of growth temperature was also explored in the temperature range of 80 to 600°C under Ga-rich and N-rich growth environments in chamber 1. Figure 9 shows the Sb content in $GaN_{1-x}Sb_x$ films as a function of growth temperature T_g under both N-rich (Ga BEP~1.6×10^{-7} T, Sb~9×10^{-8} T) and Ga-rich (Ga BEP~2.2×10^{-7} T, Sb BEP~3×10^{-8} T) conditions. We note that at constant Sb BEP, the Sb content is rather insensitive to the growth temperature over the large temperature range $60°C < T_g < 400°C$. This is particularly true for films grown under the Ga-rich condition. Note that the samples grown under N-rich conditions have a 3 times higher Sb BEP, that results in 3-4 times higher Sb content in the films. These results can be contrasted with the growth of $GaN_{1-x}As_x$ HMAs that, as also shown in Fig. 10, exhibits a stronger effect of temperature on the As content for $T_g < 400°C$. At $T_g > 500°C$ the decrease in Sb content with increasing T_g is even more pronounced when the films were grown under Ga-rich conditions. For example, at $T_g \sim 600°C$, only ~0.04% of Sb was incorporated.
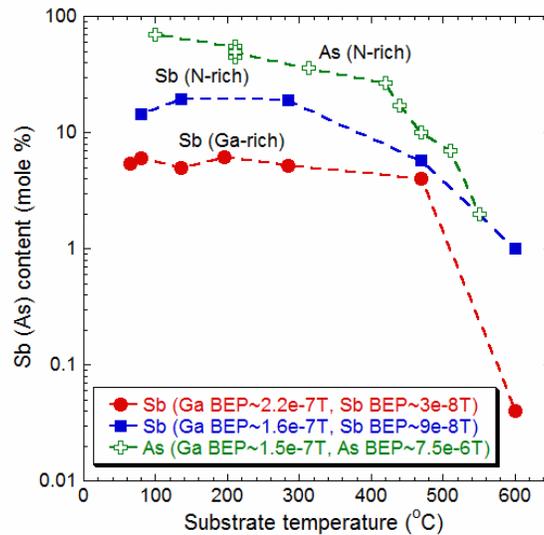

Fig. 9 Mole percent of Sb incorporated in GaN films as a function of growth temperature under both N-rich (Ga BEP~1.6×10^{-7} T) and Ga-rich (Ga BEP~2.2×10^{-7} T) conditions. The dependence of As content in $GaN_{1-x}As_x$ on growth temperature under N-rich condition is also shown for comparison. Reprinted with permission from reference [70]. Copyright 2014 AIP Publishing LLC.

GaN$_{1-x}$Sb$_x$ alloys were also grown in chamber #2 under N-rich conditions. A moderately low substrate temperature in the range of 325–550°C were used in this case. The growth rates were 0.09 μm/hr on sapphire, which is considerably slower than the growth rates used in chamber #1. The Sb mole fraction (x) as a function of Sb/N absolute flux ratio at a growth temperature of 325°C is plotted in Fig. 10. Note that since the samples were grown in two different chambers, and the flux ratios shown in Fig 8 and 9 are BEP ratios and the ratios in Fig 10 are flux ratios, a direct quantitative comparison cannot be made between these figures.

Typically, to first order, the Sb concentration can be described by $[Sb] = \frac{\Omega \Phi_{Sb}}{\Omega \Phi_{Sb} + \Omega \Phi_N}$ where Φ_{Sb} and Φ_N refer to the Sb and N flux, respectively. The interaction parameter, Ω describes the deviation from ideal incorporation. A parameter of $\Omega = 1$ describes incorporation with no interactions between the constituent atoms, where the concentration of the alloys is simply proportional to the impinging fluxes. While that is typically the case for group III-V alloys with mixed group III constituents under normal growth conditions, it is not the case for alloys with mixed group V constituents, particularly for alloys grown outside of 'normal' temperature ranges. This has been discussed at length in a prior report on the growth of InAsSb in chamber 2 [98]. The dotted lines in Fig. 10(a) shows the 'ideal' case of Sb/N ratio vs. Sb incorporation when $\Omega = 1$. For low Sb/N flux ratios of up to 0.2 (inset of Fig. 10(a)), the incorporation is well-behaved and can be described by an interaction parameter of $\Omega \sim 0.62$ (grey solid line). However, for higher Sb/N ratios it appears that the Sb composition dramatically levels off at about 18% at this growth temperature. We had been able to grow across the composition spectrum at 80°C, so it is unclear if the Sb composition is limited by the increased substrate temperature, or if it is because of the difference in absolute fluxes, etc., used in the two different MBE systems.
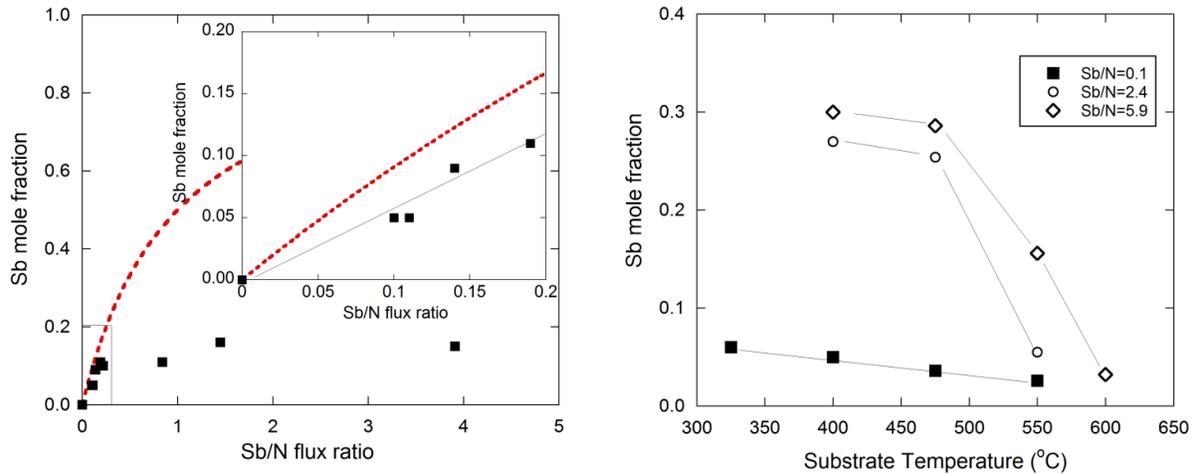

Fig. 10 (a) Sb incorporation in GaNSb as a function of Sb/N flux ratio grown at a substrate temperature 325°C. (b) Effect of substrate temperatures on the Sb incorporation for different Sb/N flux ratio. These samples were grown in chamber #2.

In general, group V incorporation is influenced by the substrate temperature in group III-V alloys with mixed group V constituents. We saw this effect in InAsSb, which showed that the Sb

incorporation decreased with increasing substrate temperatures [99]. Similarly, over a substrate temperature range of 325-600°C, the Sb incorporation decreases for fixed Sb/N conditions, as shown in Fig 10(b). Note that for a low Sb/N flux ratio (0.1) the Sb mole fraction decreases linearly with increasing T_g For the higher Sb/N ratios, however, there is a marked decrease in Sb incorporation for temperatures above 475°C. This is consistent with the results obtained on samples grown in chamber #1 as shown in Fig. 9.

4.2.2 Film Structure
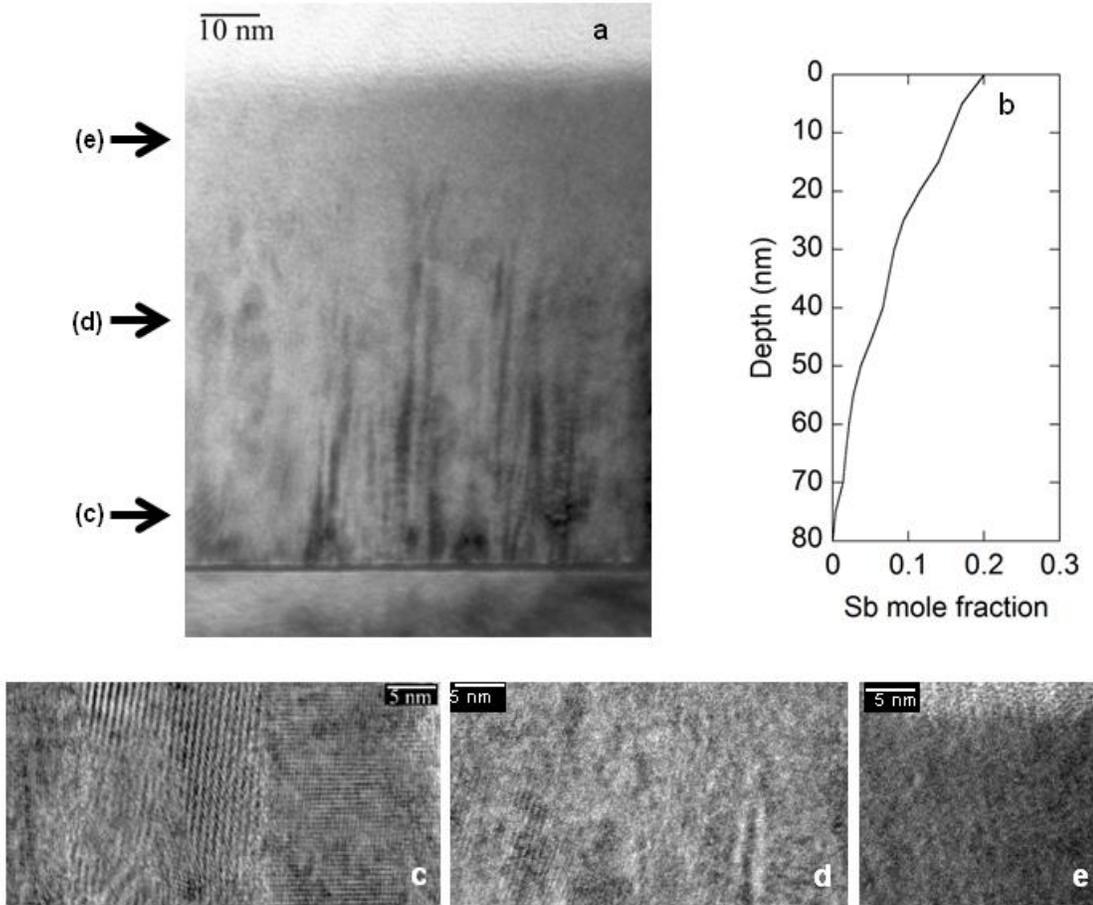

Fig. 11 Correlation of the structure revealed by cross sectional TEM and Sb composition profile measured by RBS with the Sb BEP during growth at 375°C . The high resolution TEM micrographs for different regions are shown on the left.

The effect of Sb flux on the incorporation of Sb in GaN$_{1-x}$Sb$_x$ is best illustrated in one sample grown in chamber #2 with fixed substrate temperature of 325°C, and fixed N and Ga fluxes, but varying Sb flux by gradually opening the Sb valve in equal sized steps. The Ga and N BEP were 5.18x10^{-8}and 1.48x10^{-5} Torr, respectively, nominal conditions for N-rich growth. The Sb-flux as a function of valve position was calibrated before growth by opening the valve in steps. The structure and composition was examined *ex-situ* with cross-sectional TEM and RBS

21

depth profiling. Fig 11 correlate the structural characteristics and chemical profile with the Sb BEP. The high resolution TEM cross section of the initial growth region without Sb (Fig. 11e) shows the typical columnar polycrystalline structure of GaN and low Sb-content $GaN_{1-x}Sb_x$. The growth planes are rotated within the plane, but are mostly aligned with the substrate. At the position where the RHEED intensity began to drop, the atomic depth profile shows that the $GaN_{1-x}Sb_x$ alloy contained ~5% Sb. After this point we see some interruption in the columnar pattern and slightly less preference to align with the substrate, as shown in Fig. 11d. The material is still completely polycrystalline. At the point where the Sb is 9%, most of the remaining columnar structure is lost, although most of the growth orientation preference is still evident. There is still a continuous decrease in RHEED intensity at this point. At 2570 s, where the RHEED intensity became constant, there is a complete loss of any orientation preference, and there are no long-range slip planes, so all dislocations coming from the interface with the substrate have annihilated. The Sb composition at this point is around 15%. The composition at the end of the growth was 22%. Even at this high Sb composition, the material was a poly-amorphous mix, with small crystallites present (Fig. 11c). We still did not see evidence of Sb clusters, or any Sb accumulated at the surface.

This study enables us to track growth conditions and estimate which Sb/Ga ratio is needed to obtain a single film with a specific Sb composition. We also know what morphology can be expected at that composition.
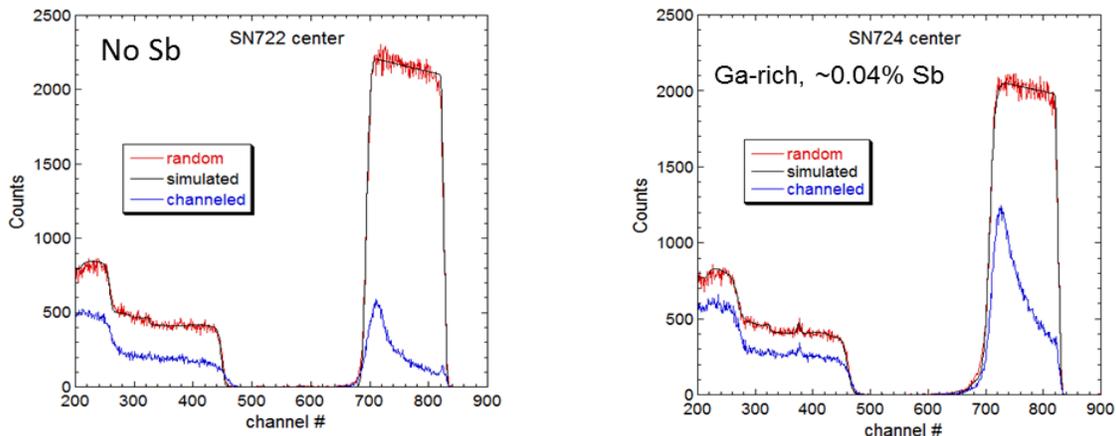

Fig. 12 Rutherford backscattering spectrometry spectra from GaN_xSb_{1-x} with (a) x=0 and (b) x=0.0004 obtained under both random (red) and channeled <0001> directions (blue).

As observed in Fig. 9 for samples grown in chamber #1, alloys grown at relatively high temperature of ~600°C can only incorporate 0.04-1% Sb, similar to results shown in Fig. 10 for alloys grown in chamber #2. XRD and ion channeling results showed that these dilute alloys grown at ~600°C still have good crystallinity. For example, as shown in Fig. 12, samples with 0.04% Sb showed a minimum channeling yield ~0.18 as compared to ~0.04 for GaN films grown under similar conditions. A much more rapid dechanneling rate is also observed in the sample with 0.04% Sb, indicating that the material has a much higher density of extended defects as compare to the undoped sample. This suggests that even very small amount of Sb atoms strongly disrupt the crystallinity of the GaN lattice.
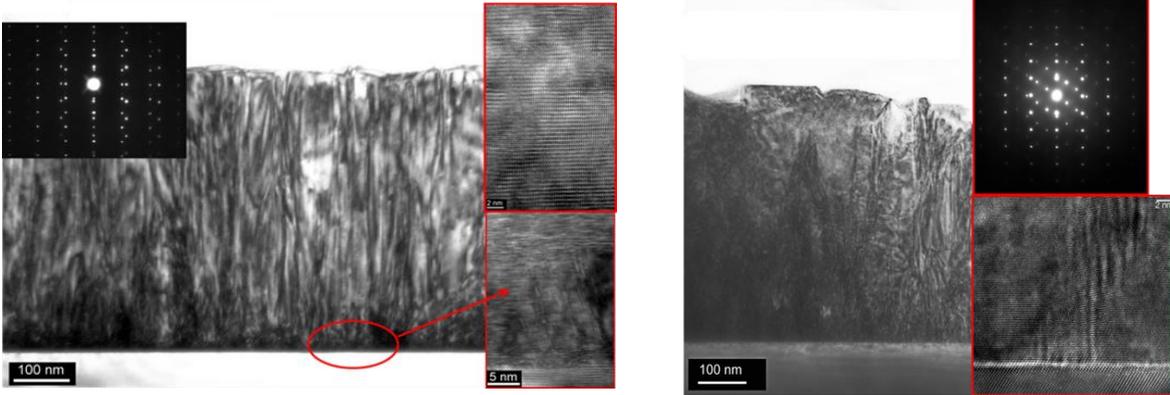
Fig. 13 TEM images of a (a) GaN film and a (b) GaN_xSb_{1-x} film with ~0.04% Sb grown at ~600°C under Ga-rich condition (Ga BEP~2.3x10^{-7} T). Selected area electron diffraction patterns are also shown in the insets of the corresponding figures. Reprinted with permission from reference [70]. Copyright 2014 AIP Publishing LLC.

The microstructure of dilute GaN_xSb_{1-x} alloys grown at relatively high temperature of 600°C are further studied by high resolution cross sectional TEM measurements. Figure 13 shows the microstructures of the two films shown in Fig. 12. For the undoped GaN film, we observe a regular columnar structure, similar to that shown in Fig. 11. The high resolution image shows that this undoped layer has good crystallinity with a higher density of defects close to the GaN/sapphire interface. In contrast, the film grown with only 0.04% of Sb shows a non-columnar structure with high dislocation density. This is in good agreement with the ion channeling results shown in Fig. 12.
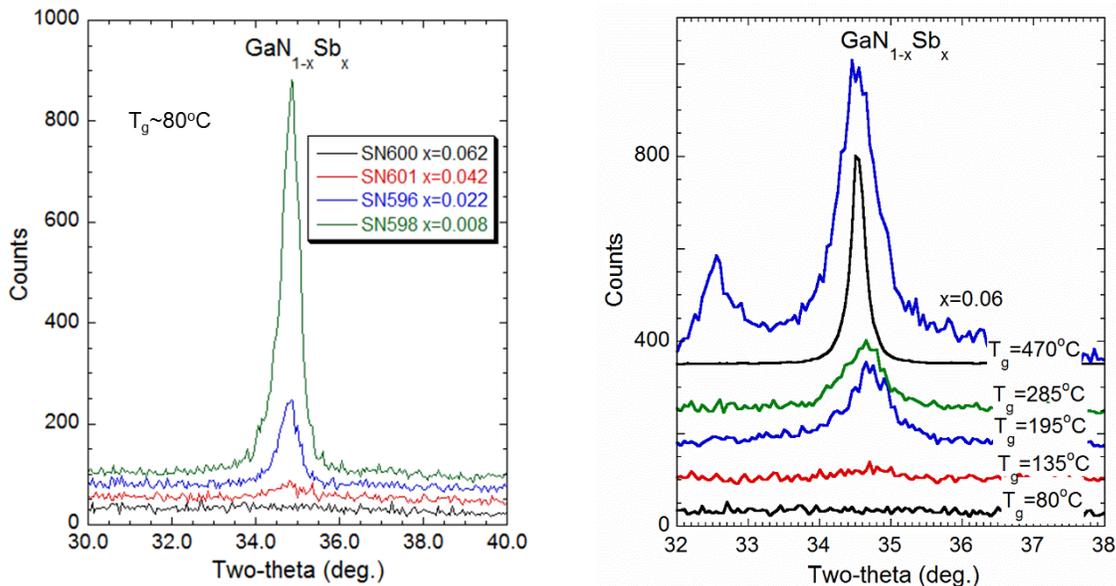

Fig. 14 (0002) XRD peak from $GaN_{1-x}Sb_x$ sample grown at (a) 80°C with different Sb content and (b) different substrate temperature with similar Ga and Sb BEP with Sb content ~4-5%.

It has been previously discussed in section 2.2 that due to the strong ionic nature of GaN, a c-axis oriented polycrystalline hexagonal GaN phase dominates even at the lowest growth temperature of 80°C [39,41,70,71,100]. As shown in Fig. 9 and 10, at this low growth temperature, more Sb can be incorporated in the GaN_xSb_{1-x} film as the Sb flux increases. XRD measurements (Fig. 14 (a)) showed that at the growth temperature of 80°C the samples become less crystalline with increasing Sb content and eventually become entirely amorphous with >~5 % of Sb. Fig. 14 (b) shows (0002) diffraction peaks of $GaN_{1-x}Sb_x$ samples grown at different substrate temperatures with similar Ga and Sb BEP and with Sb content of ~4-5.5%. At this Sb content, films grown below 100°C are entirely amorphous. At T_g~135°C the film becomes partially crystalline as evidenced by the weak and broad (0002) diffraction peak. This diffraction peak is most likely coming from small crystalline grains within the amorphous matrix. At higher growth temperatures the (0002) peak intensity increases, indicating that a larger fraction of the film is crystalline with larger grain sizes. At the even higher growth temperature of 470°C, the (0002) diffraction peak becomes strong, suggesting growth of a fully crystalline film that is preferentially oriented to the growth direction of the substrate. However at a higher Sb content of ~7 %, the films remain amorphous even for a growth temperature as high as 285°C. Phase separation occurs at the high growth temperature of 470°C when the Sb content increases to x>0.06 with a clearly visible (210) zinc blende GaSb peak at 2θ ~32.6° as shown in the top scan of Fig. 14 (b).

(a)   (b)   (c)
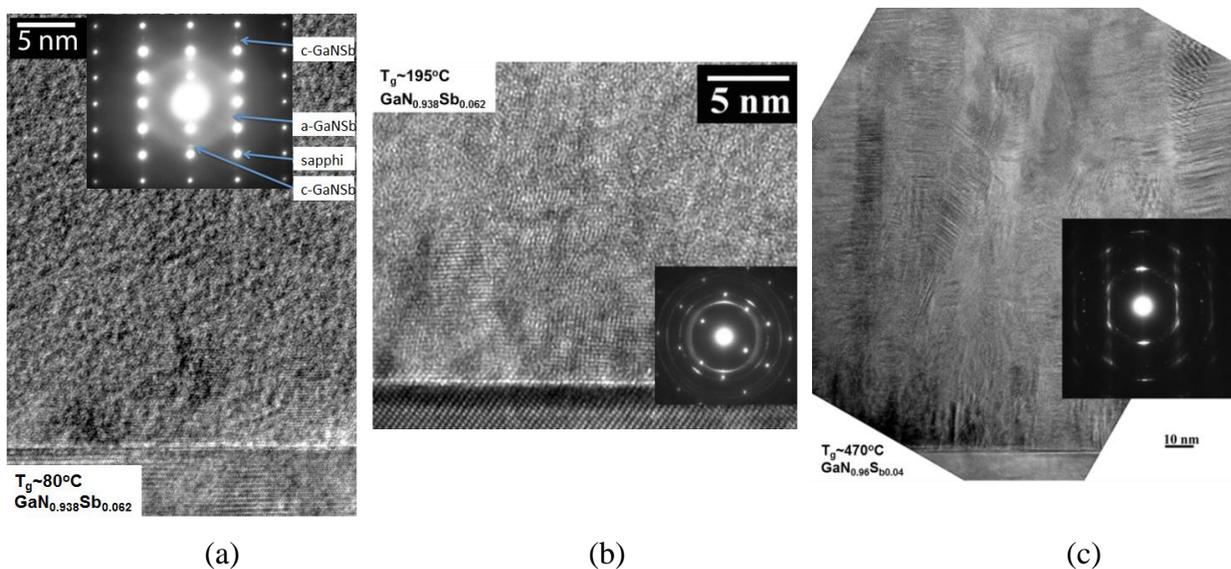
Fig. 15 Cross section TEM images and SAD patterns of samples grown at (a) 80°C (b) 195°C and (c) 470°C grown with similar Ga and Sb flux with Sb content in the range of 4-6%. Reprinted with permission from reference [70]. Copyright 2014 AIP Publishing LLC.

Cross sectional TEM images and SAD patterns for samples grown at (a) 80°C (b) 195°C and (c) 470°C with similar Ga and Sb fluxes and with Sb content in the range of 4-6% are shown in Fig. 15. At the low growth temperature of 80°C, the sample with 6.2% Sb appears to be entirely amorphous. The columnar structure that was observed in the sample with lower Sb content is completely absent in this film. The diffuse rings in the SAD pattern shown in Fig. 15(a) confirm that the film is primarily amorphous, in good agreement with the XRD results.

The microstructure of the film with 6.2 % Sb grown at 195°C shown in Fig. 15(b) reveals that the film has both crystalline grains of ~5 nm size and amorphous regions. SAD patterns also show crystalline diffraction rings indicating polycrystalline grains as well as an amorphous ring. These results are consistent with the XRD pattern of the sample showing only a weak (0002) GaN_xSb_{1-x} diffraction peak. At the high growth temperature of 470°C, both the TEM image and the SAD pattern indicate a polycrystalline film (Fig. 15(c)). From the thickness measured by cross-sectional TEM and the areal density from RBS, we calculated the density of the amorphous $GaN_{1-x}Sb_x$ film with ~6% Sb to be ~84% of the corresponding crystalline phase.

4.2.3 Effect of growth stoichiometry

Sb incorporation and the overall III:V ([Ga]/([N]+[Sb])) ratio depends quite strongly on the Ga flux during growth, particularly at low growth temperature. Fig. 16 shows the Ga flux dependence on the Sb concentration in mole % and the III/V atomic ratio, [Ga]/([Sb]+[N]) of $GaN_{1-x}Sb_x$ films grown at substrate temperature of 80°C at a fixed Sb BEP of 3.2×10^{-8} Torr in chamber #1. As is seen in Fig. 16, increasing Ga flux at a fixed Sb flux results in decreased Sb incorporation and a corresponding increase in the III/V ratio of the film. Under these growth conditions, stoichiometric III:V material with Sb mole fractions of x~0.05 can be obtained with a Ga flux of ~2×10^{-7} Torr.
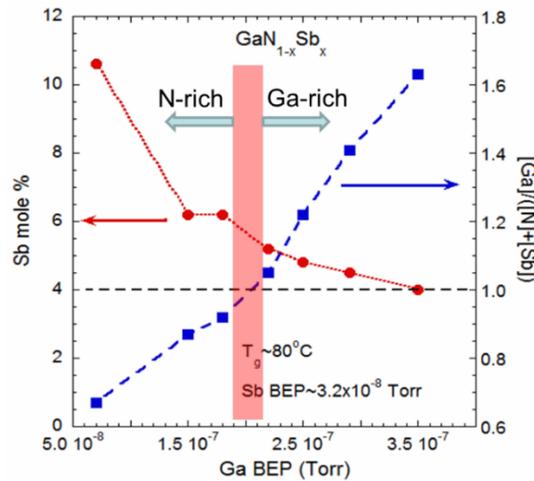

Fig. 16 Concentrations of Sb in mole % together with the III/V atomic ratio, [Ga]/([Sb]+[N]) of the films grown at substrate temperature of 80°C at a fixed Sb BEP of 3.2×10^{-8} T with increasing Ga flux.

Figure 17(a) and (b) show the Sb incorporation and III:V ratio for $GaN_{1-x}Sb_x$ films grown at a substrate temperature of 80°C with increasing Sb BEP under N-rich (Ga BEP~1.6×10^{-7} Torr) and Ga-rich (Ga BEP~2.2×10^{-7} Torr) conditions, respectively. Note that at the low growth temperature T_g~80°C the incorporation of Sb increases linearly with Sb BEP independent of the Ga BEP. Under the Ga-rich growth condition, $GaN_{1-x}Sb_x$ films with III:V ratio of unity can be obtained with Sb BEP up to 8×10^{-8} Torr with up to 10 mole % Sb. However, under N-rich growth condition, stoichiometric films can be obtained only for Sb BEP~2×10^{-8} Torr, giving rise to ~4 mole % of Sb in the film. This suggests that Ga-rich growth conditions are required to incorporate high concentrations of Sb into $GaN_{1-x}Sb_x$ while still maintaining a good film stoichiometry. However, for low Sb flux, a Ga-rich growth may also favor the incorporation of

Ga antisites Ga_N. Such Ga_N antisites may introduce deep levels within the gap as previously discussed in the LT-GaN materials.

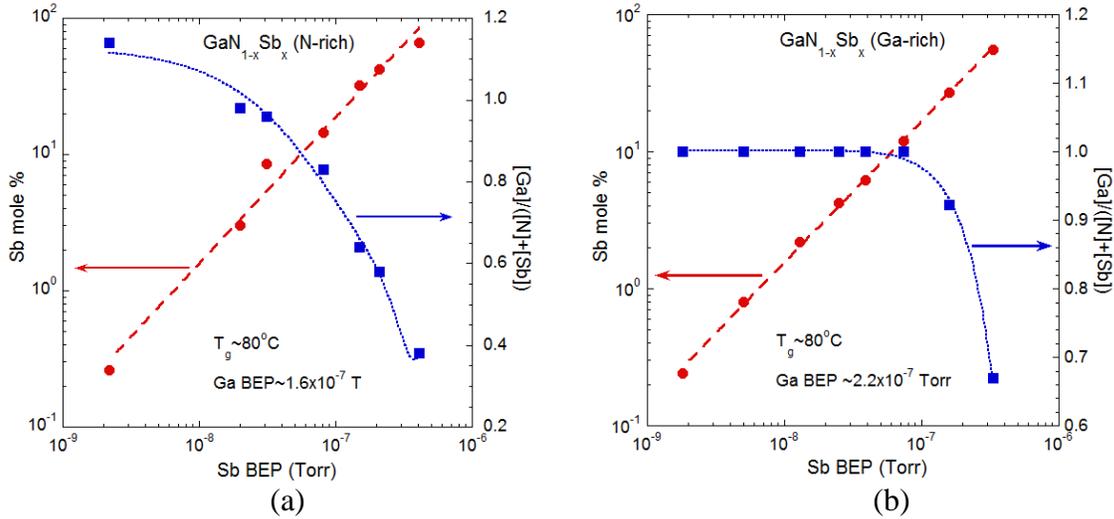(a)   (b)

Fig. 17 Concentrations of Sb in mole % together with the III/V atomic ratio, [Ga]/([Sb]+[N]) of the films grown at substrate temperature of 80°C (a) with increasing Sb flux for N-rich (Ga BEP~1.6x10^{-7} T), and (b) Ga-rich (Ga BEP~2.2x10^{-7} T) conditions. Reprinted with permission from reference [70]. Copyright 2014 AIP Publishing LLC.

4.3 Electronic properties

As discussed in section 2, electronic band structures of HMAs can be described by the anticrossing interactions between impurity localized states and the extended states of the host matrix. For GaN$_{1-x}$Sb$_x$ HMAs, the approximate location of the Sb level in GaN can be deduced from its known position at 1.0 eV below the VBM of GaAs [44]. Considering that the valence band edge offset between GaAs and GaN equals 2 eV, this places the Sb level at about 1 eV above the VBM of GaN. We utilize the GaN$_x$Sb$_{1-x}$ samples with dilute Sb impurity grown at 600°C to better locate the position of the Sb level in GaN.

Room temperature cathodoluminescence (CL) measurements on Sb doped GaN samples with dilute amount of Sb (<1%) grown at 600°C showed a broad luminescence at 2.0-2.5 eV with peak intensity at ~2.2 eV [101]. We note that only the band edge luminescence of ~3.4 eV is observed for the sample grown at similar conditions but without Sb. This suggests that the broad CL peak can be attributed to incorporation of the Sb. Wu et. al. [29] have shown that the composition dependence of the bandgap in GaNAs alloys can be explained by the BAC model with the localized As level E_{As} ~0.62 eV above the VBM of GaN. Photoluminescence measurements on As doped GaN by Foxon et al. showed a broad luminescence from 2.23 to 2.9 eV with peak intensity at ~2.65 eV [73]. Considering a likely ~0.1 eV Stokes shift in the PL peak, this places the E_{As} ~ 0.65 eV, in good agreement with the value obtained by Wu et al. Since the electronegativity difference between Sb and N is larger than between As and N, it is expected that Sb-derived localized levels lie higher above the valence band edge than that the As levels. Again, assuming the Stokes shift of 0.1 eV places the Sb level at E_{Sb} ~ 1.1 eV above the VBM of GaN. This is in a good agreement with the value extrapolated from the position of the

Sb level at 0.9 eV below the VBM in GaAs [44]. However, it is important to note that the CL peak at 2.2 eV coincides with the commonly observed "yellow" luminescence in GaN that has been attributed to native defects or defect complexes. Since incorporation of Sb affects the crystalline quality of the films it is therefore possible that Sb levels and native defects contribute to the observed CL.

4.3.1 Optical absorption

The absorption coefficient α of $GaN_{1-x}Sb_x$ films was measured using transmission and reflection measurements. Figure 18(a) shows α for $GaN_{1-x}Sb_x$ films with increasing Sb content grown at 80°C under N-rich growth condition grown in chamber #1. The absorption coefficient for a sample with x=0.062 grown under Ga-rich sample is also shown. A monotonic increase of the sub-bandgap optical absorption starting with photon energies of less than 2 eV is observed with increasing Sb content. This absorption can be attributed to optical transitions from the Sb-derived band (E_+) to the conduction band. It is very weak at low Sb concentrations but starts to dominate when the Sb content reaches a few mole %. Note that although the film becomes amorphous for x >0.07, the optical absorption shows a well-developed, relatively sharp absorption edge. In contrast, a $GaN_{1-x}Sb_x$ (x=0.062) film grown under Ga-rich conditions (Ga BEP >2.2x10^{-7} T) exhibits a strong absorption at energy as low as 1 eV. This is believed to originate from Ga_N related defect band, consistent with our investigation on the optical properties of LT-GaN [71].
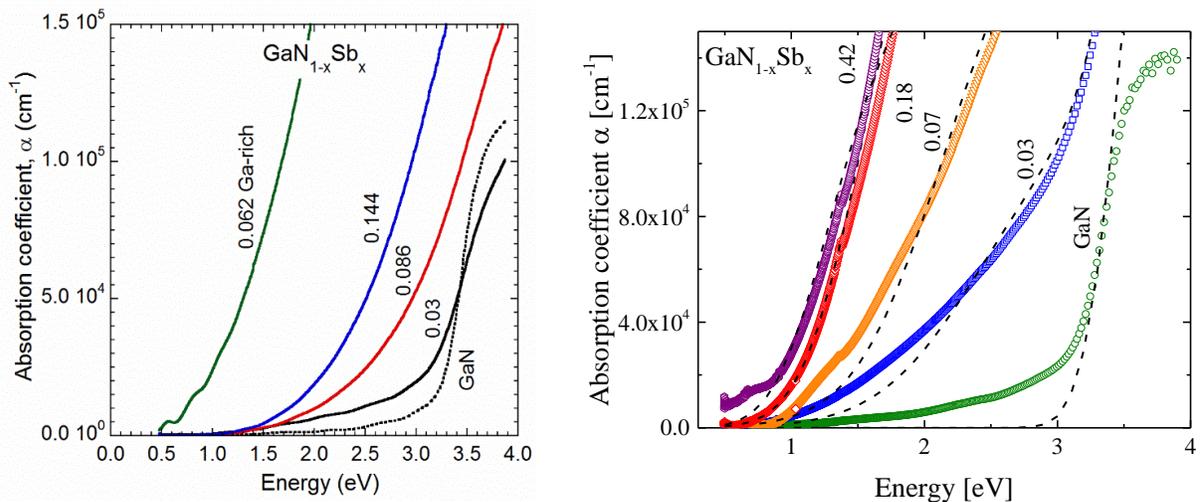

Fig. 18 Absorption coefficient, α for $GaN_{1-x}Sb_x$ films with increasing Sb content grown at (a) 80°C under N-rich growth condition grown in chamber #1 and (b) 325°C in chamber #2 by growing a multilayer structure with a number of alternating layers of GaN and GaSb. The absorption coefficient for a sample with x=0.062 grown under Ga-rich sample is also shown in 18 (a). Reprinted with permission from reference [46]. Copyright 2015 AIP Publishing LLC.

Fig, 18(b) shows the absorption coefficient of a series of $GaN_{1-x}Sb_x$ films grown in chamber #2 at a higher temperature of 325°C by growing a multilayer structure with a number of alternating layers of GaN and GaSb. An intermixing of the layers produced alloys with thicknesses of 150 - 300 nm and Sb compositions up to x = 0.42. Using this technique we were able to grow $GaN_{1-x}Sb_x$ HMAs with x up to ~0.4 at higher temperature without phase separation.

The average composition of the alloys was controlled by the GaN to GaSb layer thickness ratio. Fig. 18(b) shows that even for the sample with no Sb, the absorption spectra does not have a sharp onset. This is consistent with our previous studies of LT-GaN under Ga-rich conditions [71]. Since the thin films are grown in chamber #2 are under slightly Ga-rich conditions, we associate the absorption tail with similar type of *GaN* related defects as seen in the absorption spectra for the GaN$_{1-x}$Sb$_x$films grown by LT-MBE under Ga-rich conditions in Ref. 71. However, in contrast to the earlier studied Ga-rich samples, as the Sb fraction is increased the absorption coefficient increases and the sub-band gap absorption edge shifts to lower energies and becomes more dominant at higher Sb contents. This behavior was similar to N-rich grown samples shown in Fig. 18(a), despite the very different growth methods.

4.3.2 Electronic band structure

The electronic band structures of the GaN$_{1-x}$Sb$_x$ were calculated using the modified BAC model described in section 2.2. As mentioned previously, the simplest way to extend the BAC model was to compositionally weight the BAC results obtained in the dilute limits to the whole composition range [29,36,35,102]. This approach was successful in predicting overall trends but significantly overestimated the band gap reductions for alloys with mid-range compositions. The main deficiencies of the model were that it ignored the composition dependence of the coupling parameter and assumed that BAC interactions fully determine the shifts of the conduction and the valence band edges. To correct for the deficiencies we adopt here a hybrid model by using the VCA on the valence and conduction matrix band edges as well as on the potential of the anion lattice site [46]. Hence the coupling parameters for GaN$_{1-x}$Sb$_x$ are not constant but vary with composition. This allows the BAC interactions to be treated as perturbations. The detail of this modified BAC model has been presented in section 2.2.

At the same time we note that using the conventional method of linearly fitting α^2 as a function of photon energy to obtain the band gap cannot be applied at low Sb levels because of the complex, composition-dependent valence band structure. Since the optical absorption coefficient is proportional to the joint optical density of states and the dipole matrix element between initial and final states, six optical transitions from three valence to two conduction sub-bands have to be taken into account. We consider optical transitions from three valence bands to the conduction band: the Sb derived impurity band ($E_+^V(k)$), Sb spin orbit split band (E_+^{SO}) and the GaN matrix-like band ($E_-^C(k)$). Also, to account for broadening in the bands inherent to the BAC model and arising from localized composition fluctuations, we convolve the energy dependent joint optical density of states with a Gaussian function at each k value. The fitting procedure used here is similar to that used by Mayer et al. to evaluate the absorption coefficient in ZnO$_{1-x}$Se$_x$ HMA alloys [35]. For example, the optical absorption coefficient associated with transitions from the higher valence band $E_+^V(k)$ to the lower conduction band $E_-^C(k)$ is proportional to the corresponding joint density of states and can be written as:

$$g_+^-(\hbar\omega) = \frac{1}{4\pi\sqrt{\pi}(\Delta_C^-+\Delta_V^+)} \int \sin\left(\frac{\theta_V}{2}\right)^2 \sin\left(\frac{\theta_C}{2}\right)^2 \times \exp\text{-}\left(\frac{\hbar\omega\text{-}[E_-^C(k)\text{-}E_+^V(k)]}{\Delta_C^-+\Delta_V^+}\right)^2 k^2 dk \qquad (8)$$

where Δ_C^- and Δ_V^+ are the broadening parameters of $E_-^C(k)$and $E_+^V(k)$, respectively. In addition we have assumed that there is no optical coupling between extended and localized states, so that the optical absorption is proportional to the delocalized part of the wavefunction of a given sub-

band. This effect is accounted for by the first two factors under the integral in the above equation.

$$\theta_V(k) = \tan^{-1}\left(\frac{2C_{Sb}(x)x^2}{E(k)-E_{Sb}}\right) \text{ and } \theta_C(k) = tan^{-1}\left(\frac{2C_N(x)x^2}{E(k)-E_N}\right), \qquad (9)$$

where $C_{Sb}(x)$ and $C_N(x)$ are the composition dependent coupling parameters of the localized Sb level (E_{Sb}) with the valence band and N level (E_N) with the conduction band, respectively for GaN$_{1-x}$Sb$_x$. The expression for the total absorption coefficient includes the six transitions described above, with each transition i weighted by its degeneracy factor g_i as $\sum_{i=1}^{6} \alpha_o g_i g_i(\hbar\omega)$, where α_o is a scaling constant obtained by fitting the experimental absorption spectrum.

Figure 19(a) shows the band structure of a GaN$_{0.82}$Sb$_{0.18}$ alloy calculated using our modified BAC model. Here E_{Sb} is at 1.2 eV above the VBE of GaN, E_N at 0.45 eV above the CBE of GaSb; a coupling parameter of 2.7 eV for the N localized level with the conduction band of GaSb and 2.5 eV for the Sb level with the valence band of GaN were used [88,70]. Since the p-like states of elemental Sb have a relatively large spin-orbit splitting energy of 0.75 eV [103,104] the optical transitions from this band is considered as well. The band gap energy for the alloys are defined as the lowest transition energy between the $E_+^V(k)$ and the $E_-^C(k)$ bands. Fig. 19(b) shows the total absorption coefficient for the GaN$_{0.82}$Sb$_{0.18}$ thin film along with the six different contributions as calculated from equation (8).

Fig. 19(a) The band structure of a GaN$_{0.82}$Sb$_{0.18}$ alloy calculated using our modified BAC model. The dotted lines indicate the localized levels of the N and the Sb atoms as well as the Sb spin-orbit level. The dashed lines show the dispersions of the valence, conduction and the spin-orbit split-off band of the host matrix. (b) The black dashed line represents the calculated absorption coefficient α for the GaN$_{0.82}$Sb$_{0.18}$ film using our modified BAC model. The contributions of the six different optical transitions are also shown. Reprinted with permission from reference [46]. Copyright 2015 AIP Publishing LLC.

29

The total calculated absorption coefficients for samples with different composition using the above approached are also shown as dashed lines in Fig. 19 (b). Fitting the experimental data yields the coupling parameter of 2.5 eV for the Sb level with the GaN valence band states with broadening parameters varying from 0.01 to 0.5 eV. The obtained band gap energies for these samples, both from chamber #1 and #2 are shown in Fig. 20. Band gap values from GaSb-rich GaNSb from Ref. 88 are also included in the plot along with the composition dependence of the band gap predicted by the original BAC model, i.e. with composition independent coupling parameters as presented in Ref. 70. Positions of the CBE and the VBE predicted by the two models are shown in the inset of Fig. 20. As can be seen in the figure, the modified model provides a much better fit to the experimentally determined gaps and predicts a smaller downward shift of the CBE as a function of Sb content.
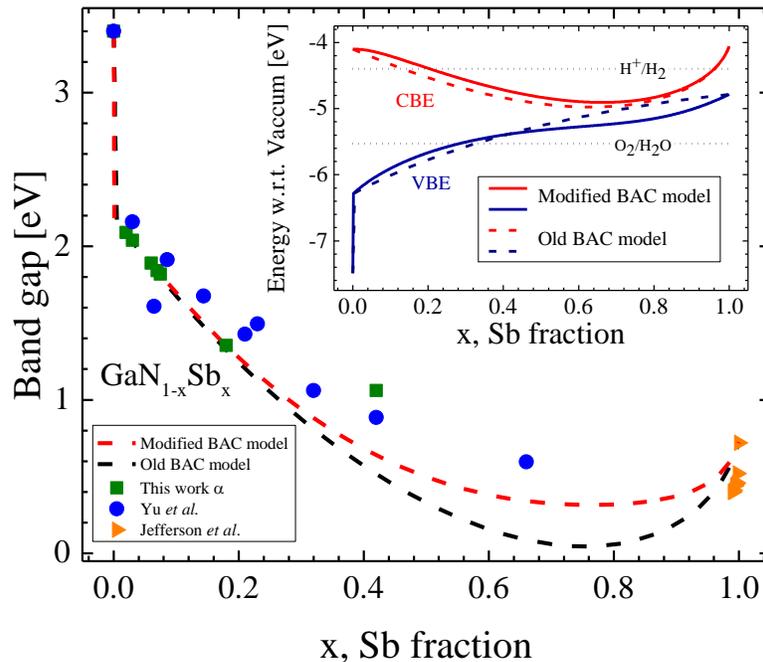

Fig. 20. Fitted bandgap energies for the $GaN_{1-x}Sb_x$ films. Band gap energies for GaSb-rich alloys with up to 1 % of N were taken from Jefferson *et al.*[88] The band gap energy over the whole composition range was calculated using our modified BAC model (dashed red line) and compared to the band gap calculated using the old model in Ref. 2 (black dashed line). The inset shows the VBE and CBE over the whole composition range using both our modified BAC model (solid line) and the old BAC model (dashed line). The Redox levels for pH = 2 are indicated as dotted lines. Reprinted with permission from reference [46]. Copyright 2015 AIP Publishing LLC.

Fig. 20 shows that the calculated bandgap dependence on composition is in very good agreement with the experimental values, especially for Sb contents <30%. For samples with Sb content >30%, the calculated values are consistently smaller than the experimental values. This can be attributed to the fact that RBS measures the total Sb concentration that may be higher than the actual amount of Sb substituting the N site and contributing to the modification of the band structure of the alloy. This difference is expected to be more severe for high Sb contents. It should also be noted that the strong decrease in the bandgap of dilute Sb alloys is associated with a large, discontinued upward shift of the VBM from the VBE of GaN to E_+ subband originating

30

from the localized Sb levels in $GaN_{1-x}Sb_x$. As is seen in the inset of Fig. 20 the large drop of the absorption edge energy (from 3.4 to ~2.3 eV) is already observed for films with only a small amount of Sb (~3 %).

5. Potential Applications

The direct conversion of sunlight into hydrogen by photoelectrochemical (PEC) water-splitting is one of the simplest methods to convert solar energy into a storable fuel. The practical realization of this technology depends critically on the availability of a suitable electrode material that combines acceptable solar response and efficiency and sufficient service lifetime for energy payback. For efficient hydrogen production by PEC water splitting, an ideal photoelectrode must meet three basic criteria: corrosion stability, a band gap small enough to absorb a significant fraction of the solar spectrum, and band edges straddling the hydrogen and oxygen redox potentials located, respectively at ~4.5 and 5.7 eV below the vacuum level [82,83]. To date, no known material satisfies all these requirements. Several oxides, most notably TiO_2, have shown good corrosion stability under operation, but have low efficiencies due to their wide band gaps [83,105,106]. III-V and II-VI semiconductors, such as $GaInP_2$ [107], have shown high water-splitting efficiencies but these materials have poor corrosion resistance and showed performance degradation and/or short lifetimes.

GaN is a mechanically hard and corrosion resistant semiconductor with CBE and VBE straddling the redox potential and hence can be a good candidate as photoelectrodes for PEC applications. However, the band gap of GaN is too large and therefore can only absorb the UV part of the solar spectrum. For GaN to be useful for PEC, its bandgap has to be significantly reduced to < 2 eV. In addition, because of the very low location of the VBE at almost 2 eV below the water oxidation potential the required band gap reduction has to be realized by an upward shift of the valence band rather than downward shift of the CBE. As is seen in Fig. 20 this goal can achieved by incorporation of Sb into GaN as it provides a method to engineer not only the band gap but also the band offsets. Specifically incorporation of even small amounts of Sb results in large upward shift of the VBE. This offers a potential of using $GaN_{1-x}Sb_x$ as a semiconductor for photoelectrochemical (PEC) water dissociation.

As can be seen from the inset of Fig. 20, the modified BAC model predicts that for $GaN_{1-x}Sb_x$ HMAs the band edges still straddle the redox potential for a composition x up to 0.2. This corresponds to a band gap of about 1.3 eV. This allows for a large flexibility in selecting alloy composition most suitable for PEC application.

However, for photoelectrode applications, controllable electrical properties of the GaN based HMAs are desired. For $GaN_{1-x}As_x$ alloys, we have demonstrated that both n and p-type doping of the material with Te and Mg, respectively can be achieved. Given the similarity of the two alloy systems, the bipolar doping of $GaN_{1-x}Sb_x$ is expected to be achievable. However, a detailed studied on the doping behaviour of $GaN_{1-x}Sb_x$ has not been carried out to date.

As we have described in this review the growth parameter space for the incorporation of As or Sb in GaN is very large. As or Sb do not incorporate substitutionally under the high-temperature growth conditions that have been found to produce high quality GaN. We must

therefore find other growth regimes that will enable incorporation while also producing material with optical and electrical properties that will enable functioning devices. The optical properties in particular seem challenging.

It is of course not obvious that *any* growth conditions achievable with MBE will result in substitutional incorporation of the larger group V atoms in GaN. Thus the systematic exploration of the parameter space is likely to be very time consuming even with the ramping experiments that we have introduced. It is therefore interesting to consider numerical growth incorporation modeling that would allow very rapid variations of growth conditions over wide ranges. With the existing volume of experimental growth conditions and results it should be possible to adjust a model to describe those and gain confidence in its predictive capabilities.

Acknowledgments

FIGURE CAPTIONS

Fig. 1. Band splitting of (a) the valence band in GaN due to the localized Sb level and of (b) the conduction band in GaSb due to the localized N level. The arrows indicate the splitting of the band into two sub-bands. The bracket indicates the band gap of the dilute alloys. The black broken lines represent the original GaN valence band in (a) and the GaSb conduction band in (b).

Fig. 2. The $GaN_{1-x}Sb_x$ dispersion relations calculated using the modified BAC model. The dashed black lines represent the valence and the conduction band edges of the matrix using the VCA, the arrows shows the linear change with increased Sb content. The band gap is defined as the difference in energy of the E_-^C and the E_+^V band.

Fig. 3 A schematic relating different crystalline phase of $Ga_{1-x}Mn_xAs$ with MBE growth temperature. Adapted from Ohno et al. [57]

Fig. 4 TEM images of N-rich (Ga BEP~$1.6x10^{-7}$ Torr) GaN thin films grown at 80°C.

Fig. 5(a) Absorption coefficient, α for GaN films with increasing Ga BEP content grown at 80°C under different Ga flux. (b) The nitrogen *K*-edge XES (left side) and total fluorescence yield XAS (right side) of GaN films grown at 80°C with different Ga BEP and a standard GaN thin film grown by plasma assisted MBE at ~800°C. The threshold-excited elastic emission peak near 396 eV was used to align the XES spectra to the XAS. The inset is a schematic diagram showing the possible location of the Ga antisites in GaAs and GaN.

Fig. 6 (a) A series of selective area diffraction patterns (SAD) patterns from $GaN_{1-x}As_x$ alloys with increasing As content as a result of decreasing growth temperature from 550 to 100°C. (b) A cross-sectional TEM micrograph of an amorphous $GaN_{1-x}As_x$ film (x=0.45; T_g=210°C).

Figure 7 (a) Photomodulated reflectance (PR) spectra from $GaN_{1-x}As_x$ thin films on a Pyrex substrate with x in the range of 0.15 to 0.45. The inset shows a comparison between the PR and absorption spectra from a $GaN_{0.76}As_{0.24}$ sample. (b) Band gap energy as a function of As content x for $GaN_{1-x}As_x$ alloys. Band gap values from both crystalline and amorphous alloys grown on sapphire and Pyrex are shown together with results from reported crystalline As-rich and N-rich $GaN_{1-x}As_x$ alloys (from references 3,11 and 29). Calculated composition dependence of the band gap of $GaN_{1-x}As_x$ alloys based on the BAC is also shown.

Fig. 8 Incorporation of Sb in GaNSb as a function of Sb flux for both Ga-rich and N-rich growth conditions at 80°C.

Fig. 9 Mole percent of Sb incorporated in GaN films as a function of growth temperature under both N-rich (Ga BEP~$1.6x10^{-7}$ T) and Ga-rich (Ga BEP~$2.2x10^{-7}$ T) conditions. The dependence of As content in $GaN_{1-x}As_x$ on growth temperature under N-rich condition is also shown for comparison.

Fig. 10 (a) Sb incorporation in GaNSb as a function of Sb/N flux ratio grown at a substrate temperature 325°C. (b) Effect of substrate temperatures on the Sb incorporation for different Sb/N flux ratio. These samples were grown in chamber #2.

Fig. 11 Correlation of the structure revealed by cross sectional TEM and Sb composition profile measured by RBS with the Sb BEP during growth at $375^{\circ}C$. The high resolution TEM micrographs for different regions are shown on the left

Fig. 12 Rutherford backscattering spectrometry spectra from GaN_xSb_{1-x} with (a) x=0 and (b) x=0.0004 obtained under both random (red) and channeled <0001> directions (blue).

Fig. 13 TEM images of a (a) GaN film and a (b) GaN_xSb_{1-x} film with ~0.04% Sb grown at ~$600^{\circ}C$ under Ga-rich condition (Ga BEP~$2.3x10^{-7}$ T). Selected area electron diffraction patterns are also shown in the insets of the corresponding figures.

Fig. 14 (0002) XRD peak from $GaN_{1-x}Sb_x$ sample grown at (a) $80^{\circ}C$ with different Sb content and (b) different substrate temperature with similar Ga and Sb BEP with Sb content ~4-5%.

Fig. 15 Cross section TEM images and SAD patterns of samples grown at (a) $80^{\circ}C$ (b) $195^{\circ}C$ and (c) $470^{\circ}C$ grown with similar Ga and Sb flux with Sb content in the range of 4-6%.

Fig. 16 Concentrations of Sb in mole % together with the III/V atomic ratio, [Ga]/([Sb]+[N]) of the films grown at substrate temperature of $80^{\circ}C$ at a fixed Sb BEP of $3.2x10^{-8}$ T with increasing Ga flux.

Fig. 17 Concentrations of Sb in mole % together with the III/V atomic ratio, [Ga]/([Sb]+[N]) of the films grown at substrate temperature of $80^{\circ}C$ (a) with increasing Sb flux for N-rich (Ga BEP~$1.6x10^{-7}$ T), and (b) Ga-rich (Ga BEP~$2.2x10^{-7}$ T) conditions.

Fig. 18 Absorption coefficient, $\Box$ for $GaN_{1-x}Sb_x$ films with increasing Sb content grown at (a) $80^{\circ}C$ under N-rich growth condition grown in chamber #1 and (b) $325^{\circ}C$ in chamber #2 by growing a multilayer structure with a number of alternating layers of GaN and GaSb. The absorption coefficient for a sample with x=0.062 grown under Ga-rich sample is also shown in 18 (a).

Fig. 19(a) The band structure of a $GaN_{0.82}Sb_{0.18}$ alloy calculated using our modified BAC model. The dotted lines indicate the localized levels of the N and the Sb atoms as well as the Sb spin-orbit level. The dashed lines show the dispersions of the valence, conduction and the spin-orbit split-off band of the host matrix. (b) The black dashed line represents the calculated absorption coefficient α for the $GaN_{0.82}Sb_{0.18}$ film using our modified BAC model. The contributions of the six different optical transitions are also shown.

Fig. 20. Fitted bandgap energies for the $GaN_{1-x}Sb_x$ films. Band gap energies for GaSb-rich alloys with up to 1 % of N were taken from Jefferson *et al*.[88] The band gap energy over the whole composition range was calculated using our modified BAC model (dashed red line) and compared to the band gap calculated using the old model in Ref. 2 (black dashed line). The inset shows the VBE and CBE over the whole composition range using both our modified BAC model (solid line) and the old BAC model (dashed line). The Redox levels for pH = 2 are indicated as dotted lines.

REFERENCES

1   Cardona M 1963 Optical properties of the silver and cuprous halides *Phys. Rev.* **129** 69-78

2   Van Vechten J A and Bergstresser T K 1970 Electronic structures of semiconductor alloys *Phys. Rev. B* **1** 3351-3358

3   Richardson D 1971 The Composition dependence of energy bands in mixed semiconductor systems with zincblende structures *J. Phys. C: Solid State Physics* **4** L289-291

4   Schulz S, Caro M A, Tan Lay-Theng, Parbrook P J, Martin R W, and O'Reilly E P 2013 Composition-dependent band gap and band-edge Bbowing in AlInN: A combined theoretical and experimental study *Appl. Phys. Exp.* **6** 121001-4

5   Walukiewicz W, Shan W, Yu K M, Ager J W III, Haller E E, Miotlowski I, Seong M J, Alawadhi H, and Ramdas A K 2000 Interaction of localized electronic states with the conduction Band: band anticrossing in II-VI semiconductor ternaries *Phys. Rev. Lett.* **85** 1552-1555.

6   Walukiewicz W, Alberi K, Wu J, Shan W, Yu K M, and Ager J W III, in *Physics of Dilute III-V Nitride Semiconductors and Material Systems: Physics and Technology*, edited by Ayse Erol (Springer-Verlag Berlin-Heidelberg 2008) Chapter 3.

7   Wu J, Shan W, and Walukiewicz W 2002 Band anticrossing in highly mismatched III-V semiconductor alloys *Semicond. Sci. Tech.* **17** 860-869

8   Weyers M, Sato M, and Ando H 1992 Red shift of photoluminescence and absorption in dilute GaAsN alloy lasers *Jpn. J. Appl. Phys.* **31** L853-855.

9   Baillargeon N, Cheng KY, Hofler G F , Pearah P J, and Hsieh K C 1992 Luminescence quenching and the formation of $GaP_{1-x}N_x$ in GaP with increasing nitrogen content *Appl. Phys. Lett.* **60** 2540-2542

10   Shan W, Walukiewicz W, Ager J W III, Haller E E, Geisz J F, Friedman D J, Olson J M, and Kurtz S R 1999 Band anticrossing in GaInNAs Alloys *Phys. Rev. Lett.* **82** 1221-1224

11   Uesugi K, Marooka N, and Suemune I 1999 Reexamination of N composition dependence of coherently grown GaNAs band gap energy with high-resolution x-ray diffraction mapping measurements *Appl. Phys. Lett.* **74** 1254-1256

12   Buyanova I and Chen Weimin, eds. *Physics and Applications of Dilute Nitrides* (Taylor & Francis, New York, 2004).

13   Erol A ed. *Physics of Dilute III-V Nitride Semiconductors and Material Systems: Physics and Technology* (Springer-Verlag Berlin-Heidelberg 2008).

14   Kondow M, Kitatani T, Nakatsuka S, Larson M C, Nakahara K, Yazawa Y, Okai M, and Uomi K 1997 GaInNAs: a novel material for long-wavelength semiconductor lasers *IEEE J. Sel. Topics in Quantum Elect*. **3**, 719-730.

15   Kondow M, Kitatani T, Larson M C, Nakahara K, Uomi K and Inoue H 1998 Gas-source MBE of GaInNAs for long-wavelength laser diodes *J. Crystal Growth* **188**, 255-259

16   Friedman D J, Geisz J F, Kurtz S R, Myers D and Olson J M 1998 1-eV solar cells with GaInNAs active layer *J. Cryst. Growth* **195**, 409-415

17   Kurtz S R, Allerman A A, Jones E D, Gee J M, Banas J J, and Hammons B E 1999 InGaAsN solar cells with 1.0 eV band gap, lattice matched to GaAs *Appl. Phys. Lett.* **74** 729-731.

18   López N, Reichertz L A, Yu K M, Campman K, and Walukiewicz W, 2011 Engineering the electronic band structure for multiband solar Ccells *Phys. Rev. Lett.* **106** 028701-4

19   Ahsan N, Miyashita N, Islam M M, Yu K M, Walukiewicz W , Okada Y 2012 *Appl. Phys. Lett.* **100** 172111-3

20   López N, Yu K M, Tanaka T, and Walukiewicz W 2015 Multicolor electroluminescence from intermediate band solar cell structures *Adv. Energy Mater.* 1501820

21   Bi W G and Tu C W 1996 N incorporation in InP and band gap bowing in InN_xP. *J. Appl. Phys.* **80** 1934-1936

22   Yu K M, Walukiewicz W, Shan W, Wu J, Beeman J W, Ager J W III, Haller E E, Xin H P, and Tu C W 2001 Synthesis of InN_xP_{1-x} thin films by N ion implantation *Appl. Phys. Lett.* **78** 1077-1079

23   Shan W, Walukiewicz W, Yu K M, Ager J W III, Haller E E, Xin H P, and Tu C W 2000 Nature of the Fundamental Bandgap in GaN_xP_{1-x} Alloys *Appl. Phys. Lett.* **76** 3251-3253

24   Li W, Héroux J B, and Wang W I 2003 InGaAsSbN: A dilute nitride compound for midinfrared optoelectronic devices *J. Appl. Phys.* **94** 4248-4250

25   Harmand J C, Ungaro G, Ramos J, Rao E V K, Saint-Girons G, Teissier R, Le Roux G, Largeau L, Patriarche G J 2000 Investigations on GaAsSbN/GaAs Quantum Wells for 1.3-1.55 um Emission *J. Cryst. Growth* **227-228** 553-557

26   Iyer S, Wu L, Li J, Potoczny S, Matney K, and Kent P R C 2007 Effects of N incorporation on the structural and photoluminescence characteristics of GaSbN/GaSb single quantum wells *J. Appl. Phys.* **101** 113508-5

27   Francoeur S, Seong M J, Mascarenhas A, Tixier S, Adamcyk M, Tiedje T 2003 Band gap of $GaAs_{1-x}Bi_x$, 0<x<3.6% *Appl. Phys. Lett.* **82** 3874-6

28   Huang W, Oe K, Feng G, and Yoshimoto M, 2005 Molecular-beam epitaxy and characteristics of $GaN_yAs_{1-x-y}Bi_x$ *J. Appl. Phys.* **98** 053505-6

29   Wu J, Walukiewicz W, Yu K M, Denlinger J D, ShanW , Ager J W III, Kimura A, Tang H F, Kuech T F 2004 Valence band hybridization in N-rich $GaN_{1-x}As_x$ alloys *Phys Rev B* **70** 115214-7.

30   Shan W, Walukiewicz W, Ager J W III, Yu K M, Wu J, Haller E E, Nabetani Y, Mukawa T, Ito Y, and Matsumoto T 2003 Effect of Oxygen on the Electronic Band Structure in ZnO_xSe_{1-x} Alloys *Appl. Phys. Lett.* **83** 299-301

31.   Yu K M, Walukiewicz W, Wu J, Shan W, Beeman J W, Scarpulla M A, Dubon O D and Becla P 2003 Diluted II-VI oxide semiconductors with multiple band gaps *Phys. Rev. Lett.* **91** 246203-4

32   Yu K M, Walukiewicz W, Wu J, Shan W, and Beeman J W, Scarpulla M A, Dubon O D, and Becla P 2004 Synthesis and optical properties of II-O-VI highly mismatched alloys *J. Appl. Phys.* **95** 6232-8

33   Tanaka T, Kusaba S, Mochinaga T, Saito K, Guo Q, Nishio M, Yu K M, and Walukiewicz W 2012 Molecular beam epitaxial growth and optical properties of highly mismatched $ZnTe_{1-x}O_x$ alloys *Appl. Phys. Lett.* **100** 011905-3

34   Tanaka T, Nagao Y, Mochinaga T, Saito K, Guo Q, Nishio M, Yu K M, and Walukiewicz W 2013 Molecular beam epitaxial growth of ZnCdTeO epilayers for intermediate band solar cells *J. Cryst. Growth* **378** 259-262

35   Mayer M A, Speaks D T M, Yu K M, Mao S S, Haller E E, and Walukiewicz W 2010 Band structure engineering of $ZnO_{1-x}Se_x$ alloys *Appl. Phys. Lett.* **97** 022104-3

36 Ting M, dos Reis R, Jaquez M, Dubon O D, Mao S S, Yu K M, and Walukiewicz W 2015 Tunability of electronic band structures in ZnO-rich highly mismatched $ZnO_{1-x}Te_x$ alloys *Appl. Phys. Lett.* **106**, 092101-4

37 Kent P R, Bellaiche L, and Zunger A 2002 Pseudopotential theory of dilute III-V nitrides *Semicond. Sci. Technol.* **17** 851-859

38 O'Reilly E P, Lindsay A, Tomic S, and Kamal-Saadi M 2002 Tight-binding and k·p models for the electronic structure of Ga(In)NAs and related alloys *Semicond. Sci. Technol.* **17** 870-879

39 Yu K M, Novikov S V, Broesler R, Demchenko I N, Denlinger J D, Liliental-Weber Z, Luckert F, Martin R W, Walukiewicz W, and Foxon C T 2009 Highly mismatched crystalline and amorphous alloys in the whole composition range *J. Appl. Phys.* **106**, 103709

40 Sheetz R, Richter E, Andriotis A N, Lisenkov S, Pendyala C, Sunkara M K, and Menon M 2011 Visible-light absorption and large band-gap bowing of $GaN_{1-x}Sb_x$ from first principles *Phys. Rev. B* **84** 075304

41 Yu K M, Sarney W L, Novikov S V, Detert D, Zhao R, Denlinger J, Svensson S P, Dubon O D, Walukiewicz W, and Foxon C T 2013 Highly mismatched N-rich $GaN_{1-x}Sb_x$ films grown by low temperature molecular beam epitaxy *Appl. Phys. Lett.* **102** 102104

42 Yu K M, Walukiewicz W, Scarpulla M A, Dubon O D, Jasinski J, Liliental-Weber Z, Wu J, Beeman J W, Pillai M R, and Aziz M J 2003 Synthesis of GaN_xAs_{1-x} thin films by pulsed laser melting and rapid thermal annealing (PLM-RTA) of N^+-implanted GaAs *J. Appl. Phys.* **94** 1043-1049

43 Alberi K, Blacksberg J, Bell L, Nikzad S, Yu K M, Dubon O D, Walukiewicz W 2008 Band anticrossing in highly mismatched Sn_xGe_{1-x} semiconducting alloys *Phys. Rev B* **77** 073202

44 Alberi K, Wu J, Walukiewicz W, Yu K M, Dubon O D, Watkins S P, Wang C X, Liu X, Cho Y-J, and Furdyna J 2007 Valence-band anticrossing in mismatched III-V semiconductor alloys *Phys. Rev. B* **75** 045203

45 Jaquez M, Yu K M, Ting M, Hettick M, Welna M, Javey A, Dubon O D, Walukiewicz W 2015 Band Anticrossing of Highly Mismatched $ZnO_{1-x}S_x$ Alloys Over the Entire Composition *J. Appl. Phys.* **118** 215702

46 Segercrantz N, Yu K M, Ting M, Sarney W L, Svensson S P, Novikov S V, Foxon C T, and Walukiewicz W 2015 Electronic band structure of highly mismatched alloys in a broad composition range: GaN1-xSbx *Appl. Phys. Lett.* **107** 142104

47 Ohki Y, Toyoda Y, Kobayashi H, and I Akasaki 1981 Fabrication and properties of a practical blue-emitting GaN MIS diode *Inst. Phys. Conf. Ser.* **63** 479

48 Sasaki T and Matsuoka T 1988 Substrate-polarity dependence of metal-organic vapor-phase epitaxy-grown GaN on SiC *J. Appl. Phys.* **64** 4531

49 Gaskill D K, Bottka N, and Lin M C 1986 Growth of GaN films using trimethylgallium and hydrazine *Appl. Phys. Lett.* **48** 1449-1451

50 Strite S and Morkoc H 1992 *J Vac. Sci. Technol. B* **10**, 1237-1266 and references therein

51 Ehrentraut D, Pakalapati R T, Kamber D S, Jiang W, Pocius D W, Downey B C, McLaurin M, and D'Evelyn M P 2013 High quality, low cost ammonothermal bulk GaN substrates *Jpn. J. Appl. Phys.* **52** 08JA01

52 Kucharski R, Zając M, Doradziński R, Rudziński M, Kudrawiec R, and Dwiliński R 2012 Non-polar and semi-polar ammonothermal GaN substrates *Semicond. Sci. Technol.* **27** 024007

53 Amano H 2013 Progress and prospect of the growth of wide-band-gap group III nitrides: Development of the growth method for single-crystal bulk GaN *Jpn. J. of Appl. Phys.* **52** 050001

54 DenBaars S P, Feezell D, Kelchner K, Pimputkar S, Pan C-C, Yen C-C, Tanaka S, Zhao Y, Pfaff N, Farrell R, Iza M, Keller S, Mishra U, Speck J S, Nakamura S 2013 Development of gallium-nitride-based light-emitting diodes (LEDs) and laser diodes for energy-efficient lighting and displays *Acta Materialia* **61** 945–951

55 Dimitrijev S, Han J, Moghadam H A, and Aminbeidokhti A 2015 Power-switching applications beyond silicon: Status and future prospects of SiC and GaN devices *MRS Bulletin* **40** 399-405

56 Motamedi P, Dalilib A, and Cadien K 2015 *J. Mater. Chem. C* **3** 7428-7436

57 Ohno H 1998 Making nonmagnetic semiconductors ferromagnetic *Science* **281** 951-956

58 Cho Y J, Yu K M, Liu X, Walukiewicz W, and Furdyna J K 2008 Effects of donor doping on $Ga_{1-x}Mn_xAs$ *Appl. Phys. Lett.* **93** 26250

59 Kaminska M, Liliental-Weber Z, Weber E R, George T, Kortright J B, Smith F W, Tsaur B Y and Calawa R 1989 Structural properties of As-rich GaAs grown by molecular beam epitaxy at low temperatures *Appl. Phys. Lett.* **54** 1881-1883

60 Yu K M and Liliental-Weber Z 1991 Lattice site locations of excess arsenic atoms in gallium arsenide grown by low-temperature molecular beam epitaxy *Appl. Phys. Lett.* **59** 3267-3269

61 Smith F W, Calawa A R, Chen C L, Manfra M J, and Mahoney L J 1988 New MBE buffer used to eliminate backgating in GaAs MESFETs *IEEE Electron. Lett.* **9** 77-80

62 Ma K, Urata R, Miller D, Harris J 2004 Low-Temperature growth of GaAs on Si used for ultrafast photoconductive switches *IEEE Journal of Quantum Electronics* **40** 800-804

63 Luo H, Laframboise S R, Wasilewski Z R, Aers G C, Liu H C, and Cao J C 2007 Terahertz quantum-cascade lasers based on a three-well active module *Appl. Phys. Lett.* **90** 041112

64 Z Liliental-Weber, Swider W, Yu K M, Kortright J, Smith F W, and Calawa A R 1991 Breakdown of crystallinity in low-temperature-grown GaAs layers *Appl. Phys. Lett.* **58** 2143-5

65 Bliss D E, Walukiewicz W, Ager J W, Haller E E, Chan K T, and Tanigawa S 1992 Annealing studies of low-temperature-grown GaAs:Be *J. Appl. Phys.* **71**, 1799

66 Liu X, Prasad A, Chen W M, Kurpiewski A, Liliental-Weber Z, and Weber E R 1994 Mechanism responsible for the semi-insulating properties of low-temperature-grown GaAs *Appl. Phys. Lett.* **65** 3002-4

67 Luysberg M, Sohn H, Prasad A, Specht P, Liliental-Weber Z, Weber E R, Gebauer J, and Krause-Rehberg R 1998 Effects of the growth temperature and As/Ga flux ratio on the incorporation of excess As into low temperature grown GaAs *J. Appl. Phys.* **83** 561-566

68 Young W T , Silva S R P, Anguita J V, Shannon J M, K Homewood P, Sealy B J 2000 Low temperature growth of gallium nitride *Diamond and Related Materials* **9**, 456-459

69 Ni C-J and Hong F C-N 2014 *J. Vac. Sci. Technol. A* **32** 031514

70 Yu K M, Novikov S V, Ting M, Sarney W L, Svensson S P, Shaw M, Martin R W, Walukiewicz W, and Foxon C T 2014 Growth and characterization of highly mismatched $GaN_{1-x}Sb_x$ alloys *J. Appl. Phys.* 116 123704

71 Yu K M, Novikov S V, Ting M, Collin C, Sarney W L, Svensson S P, Luce A V, Denlinger J D, Walukiewicz W and Foxon C T 2015 Effects of native defects on properties of low temperature grown, non-stoichiomtric gallium nitride *J. Phys. D* **48,** 385101 (2015).

72 Svensson S P, Sarney W L, Yu K M, Calley W L, Novikov S V, Walukiewicz W 2015 Determination of N-/Ga-rich growth conditions, using in-situ Auger electron spectroscopy," *J. Cryst. Growth* **425**, 2-4

73 Foxon C T, Harrison I, Novikov S V, Winser A J, Campion R P, Li T 2002 The growth and properties of GaN:As layers prepared by plasma-assisted molecular beam epitaxy *J. of Physics: Condensed Matter* **14** 3383

74 Kimura A, Paulson C A, Tang H F, and Kuech T F 2004 Epitaxial $GaN_{1-y}As_y$ layers with high As content grown by metalorganic vapor phase epitaxy and their band gap energy *Appl. Phys. Lett.* **84**, 1489-1491

75 Kimura A, Tang H F, and Kuech T F 2004 *J. Cryst. Growth* **265**, 71-77

76 Novikov S V, Staddon C R, Akimov A V, Campion R P, Zainal N, Kent A J, Foxon C T, Chen C-H, Yu K M, Walukiewicz W 2009 Molecular beam epitaxy of crystalline and amorphous GaN layers with high As content *J. Cryst. Growth* **311** 3417–3422

77 Yu K M, Novikov S V, Broesler R, Liliental-Weber Z, Levander A X, Dubon O D, Wu J, Walukiewicz W, and Foxon C T 2010 Low Gap Amorphous $GaN_{1-x}As_x$ Alloys Grown on Glass Substrate *Appl. Phys. Lett.* **97** 101906

78 Levander A X, Yu K M, Novikov S V, Liliental-Weber Z, Foxon C T, Dubon O D, Wu J, and Walukiewicz W 2013 Local structure of amorphous $GaN_{1-x}As_x$ semiconductor alloys across the composition range *J. Appl. Phys.* **113** 243505

79 Levander A X, Liliental-Weber Z, Broesler R, Hawkridge M E, Novikov S V, Foxon C T, Dubon O D, Wu J, Walukiewicz W, and Yu K M 2011 Thermal stability of amorphous alloys *Appl. Phys. Lett*. **98** 161902

80 Levander A X, Novikov S V, Liliental-Weber Z, dos Reis R, Dubon O D, Wu J, Foxon C T, Yu K M, and Walukiewicz W 2011 Doping of GaN1−xAsx with high As content J. *Appl. Phys*. **110** 093702

81 Novikov S V, Ting M, Yu K M, Sarney W L, Martin R W, Svensson S P, Walukiewicz W and Foxon C T 2014 Tellurium n-type doping of highly mismatched amorphous $GaN_{1-x}As_x$ alloys in plasma-assisted molecular beam epitaxy J. Cryst. Growth **404** 9-13

82 Bak T, Nowotny J, Rekas M, Sorrell C C 2002 Photo-electrochemical hydrogen generation from water using solar energy. Materials-related aspects *International Journal of Hydrogen Energy* **27**, 991-1022

83 Sorrell C C, Sugihara S, and Nowotny J Eds., *Materials for energy conversion devices* (Woodhead Publishing Limited, Cambridge, England, 2005) ISBN-10:1 85573 932 1.

84 Wang D, Svensson S P, ShterengasL, Belenky G, Kim C S, Vurgaftman I, and Meyer J R 2009 Band edge optical transitions in dilute-nitride GaNSb *J. Appl. Phys.* **105** 014904

85 Svensson S P, Donetsky D, Wang D, Hier H, Crown F J, and Belenky G 2011 Growth of type II strained layer superlattice, bulk InAs and GaSb materials for minority lifetime characterization *J. Cryst Growth* **334** 103-107

86 Nair H P, Crook A M, Yu K M, and Bank S R 2012 Structural and optical studies of nitrogen incorporation into GaSb-based GaInSb quantum wells *Appl. Phys. Lett.* **100** 21103

87 Veal T D, L. Piper F J, Jollands S, Bennett B R, Jefferson P H, Thomas P A, McConville C F, Murdin B N, Buckle L, Smith G W, and Ashley T 2005 Band gap reduction in GaNSb alloys due to the anion mismatch *Appl. Phys. Lett*. **87** 132101

88 Jefferson P H, Veal T D, Piper L F J, Bennett B R, McConville C F, Murdin B N, Buckle L, Smith G W, and Ashley T 2006 Band anticrossing in GaN_xSb_{1-x} *Appl. Phys. Lett.* **89** 111921

89 Belabbes A, Ferhat M, and Zaoui A 2006 Giant and composition-dependent optical band gap bowing in dilute $GaSb_{1-x}N_x$ alloys *Appl. Phys. Lett.* **88** 152109

90 Ashwin M J, Walker D, Thomas P A, Jones T S, and Veal T D 2013 N incorporation in GaInNSb alloys and lattice matching to GaSb *J. Appl. Phys.* **113** 033502

91 Sarney W L and Svensson S P 2009 Materials study of the competing group V element incorporation process in dilute-nitride films, *MRS Proceedings* **1202** 1202-I05-24

92 Sarney W L, Svensson S P, Hier H, Donetsky D, Wang D, Shterengas L, Suchalkin S, Belenky G 2011 New approaches to direct bandgap III-V materials for LWIR detector applications, *AIP Conf. Proc.* **1416** 59-61

93 Buckle L, Bennett B R, Jollands S, Veal T D, Wilson N R, Murdin B N, McConville C F, Ashley T 2005 Growth of dilute GaNSb by plasma-assisted MBE *J Cryt. Growth* **278** 188-192

94 Jin Y, Jock R M, Cheng H, He Y, Mintarov A M, Wang Y, Kurdak C, Merz J L, and Goldman R S 2009 Influence of N interstitials on the electronic properties of GaAsN alloys *Appl. Phys. Lett*. **95** 062109

95 Sarney W L, and Svensson S P 2013 Discrepancies in the nature of nitrogen incorporation in dilute-nitride GaSbN and GaAsN films *J. Vac. Sci. Technol. B* **31** 051206

96 Sarney W L, Svensson S P, Hier H, Kipshidze G, Donetsky D, Wang D, Shterengas L, and Belenky G 2012 Structural and Luminescent Properties of Bulk InAsSb *J. Vac. Sci. Technol. B* **30** 02B109

97 Lin Y, Wang D, Donetsky D, Shterengas L, Kipshidze G, Belenky G, Svensson S P, Sarney W L, and Hier H S 2013 Conduction- and nalence-band energies in bulk InAsSb and type II InAsSb/InAs strained-layer superlattices *J. Electron. Mater* **42** 918-926

98 Sarney W L and Svensson S P 2015 The flux dependent Sb-incorporation during molecular beam epitaxy of InAsSb *J. Vac. Sci. Tech. B* **33**, 060604

99 Sarney W L, Svensson S P, Anderson E M, Lundquist A M, Pearson C, and Millunchick J M 2014 The influence of growth temperature on Sb incorporation in InAsSb, and the temperature-dependent impact of Bi surfactants J. Cryst. Growth **406** 8-11

100 Sarney W L, Svensson S P, Novikov S V, Yu K M, Walukiewicz W, Foxon C T 2013 $GaN_{1-x}Sb_x$ highly mismatched alloys grown by low temperature molecular beam epitaxy under Ga-rich conditions J. Cryst. Growth **383** 95-99

101 Shaw M, Yu K M, Ting M, Powell R E L, Sarney W L, Svensson S P, Kent A J, Walukiewicz W, Foxon C T, Novikov S V and Martin R W 2014 Composition and optical properties of dilute-Sb $GaN_{1-x}Sb_x$ highly mismatched alloys grown by MBE *J. Phys. D: Appl. Phys.* **47** 465102

102 Zhao C-Z, Li N-N, Wei T, Wang S-S, and Lu K-Q 2014 Bandgap evolution of $GaN_{1-x}As_x$ in the whole composition range *Appl. Phys. A* **115** 927-930

103 Cardona M, Christensen N E, and Fasol G 1988 Relativistic band structure and spin-orbit splitting of zinc-blende-type semiconductors *Phys. Rev. B* **38** 1806-1827

104 Peralta J E, Heyd J, Scuseria G E, and Martin R L 2006 Spin-orbit splittings and energy band gaps calculated with the Heyd-Scuseria-Ernzerhof screened hybrid functional *Phys. Rev. B* **74**, 073101

105 Ghosh A K and Muruska H P 1977 Photoelectrolysis of water in sunlight with sensitized semiconductor electrodes *J Electrochem Soc* **124** 1516-1522

106 Akikusa J and Khan S 1997 Photoresponse and AC impedance characterization of n-TiO$_2$ films during hydrogen and oxygen evolution reactions in an electrochemical cell *Int J Hydrogen Energy* **22** 875-882

107 Khaselev O and Turner J 1998 A Monolithic photovoltaic-photoelectrochemical device for hydrogen production via water splitting *Science* **280** 425-427